Journal of Computational Physics 562 (2026) 115004

Contents lists available at ScienceDirect

Journal of Computational Physics

journal homepage: www.elsevier.com/locate/jcp

# A kernel-free boundary integral method for elliptic interface problems on surfaces

Pengsong Yin [a], Wenjun Ying [a,*], Yulin Zhang [a], Han Zhou [b,*]

[a] School of Mathematical Sciences, MOE-LSC and Institute of Natural Sciences, Shanghai Jiao Tong University, Shanghai, 200240, China
[b] Department of Mathematics, University of Pennsylvania, Philadelphia, Pennsylvania, 19104, USA

ARTICLE INFO

*2020 MSC:*
65N06
35R01
35J25

*Keywords:*
Kernel-free boundary integral method
Surface PDE
Interface problem
Fast multigrid solver
Cartesian grids

ABSTRACT

This work presents a generalized boundary integral method for elliptic equations on surfaces, encompassing both boundary value and interface problems. The method is kernel-free, implying that the explicit analytical expression of the kernel function is not required when solving the boundary integral equations. The numerical integration of single- and double-layer potentials or volume integrals at the boundary is replaced by interpolation of the solution to an equivalent interface problem, which is then solved using a fast multigrid solver on Cartesian grids. This paper provides a detailed implementation of the second-order version of the kernel-free boundary integral method for elliptic PDEs defined on an embedding surface in $\mathbb{R}^3$ and presents numerical experiments demonstrating the efficiency and accuracy of the method for both boundary value and interface problems.

## 1. Introduction

Partial differential equations (PDEs) on curved surfaces are crucial for modeling diffusive or transport phenomena on non-planar domains, such as terrestrial ocean currents [1] or the diffusion of surfactants on fluid interfaces [2,3]. These problems span multiple disciplines, including geophysics [4,5], fluid mechanics [6,7], and biophysics [8,9]. In these applications, internal sharp interfaces—co-dimension one objects—often emerge within the surfaces due to medium inhomogeneities, as exemplified by two-phase flows or phase separation processes. For instance, the strongly anisotropic Cahn-Hilliard equation serves as a fundamental model for surface phase separation, for which stable, high-order accurate numerical schemes have recently been developed [10,11]. The presence of sharp interfaces divides the surface into distinct subdomains, across which the solution is piecewise smooth. Consequently, this paper proposes an efficient numerical method to address elliptic PDE interface problems on surfaces.

Considerable research has recently been conducted on the development and analysis of numerical methods for solving surface PDEs. Due to the geometric intricacies introduced by the underlying surface, numerical methods are fundamentally categorized as either intrinsic or extrinsic. Intrinsic approaches involve formulating the PDE by globally or locally parameterizing the surface, followed by the discretization of the surface PDE within the parameter space. These approaches encompass surface triangular mesh-based methods, such as surface finite element methods [12–14], finite volume methods [15,16], and strategies that involve locally parameterizing the surface by introducing overlapping patches [17–19]. These techniques do not rely on the embedded space, with the computational mesh confined to the surface itself, thereby offering enhanced accuracy and efficiency. Conversely, extrinsic methods

---

* Corresponding authors.
*E-mail addresses:* yps2701155@sjtu.edu.cn (P. Yin), wying@sjtu.edu.cn (W. Ying), yulin.zhang@sjtu.edu.cn (Y. Zhang), hzhou24@sas.upenn.edu (H. Zhou).

https://doi.org/10.1016/j.jcp.2026.115004
Received 23 August 2025; Received in revised form 10 April 2026; Accepted 1 May 2026
Available online 9 May 2026

involve embedding the surface into an expanded Euclidean space and extending the solution to the PDE beyond the surface. This category includes the closest point method [20,21], the narrow band finite element method [22,23], and the trace finite element method [24,25]. The extended solution typically satisfies a simplified PDE, facilitating easier numerical discretization. Moreover, straightforward computational meshes can be generated in the Euclidean space without necessitating alignment with the complex surface.

For the solution of PDEs with interfaces, the inherent lack of smoothness at sharp interfaces leads to a loss of convergence and accuracy for standard discretizations. The jump conditions can be addressed through the employment of an interface-fitted computational mesh. Nonetheless, generating such high-quality fitted triangular meshes poses a non-trivial and time-consuming challenge. Consequently, extensive research over recent decades has concentrated on the development of unfitted mesh-based methods for solving interface problems. This encompasses finite difference-type methods, such as the immersed interface method [26,27], the matched interface and boundary method [28,29], and the kernel-free boundary integral method (KFBI) [30–32], as well as finite element-type approaches, including the immersed finite element method [33,34]. Unfitted mesh-based methods permit the interface to traverse mesh nodes and utilize local strategies to accurately handle the solution jump at the interface while preserving global convergence and efficiency.

There is a paucity of studies concerning numerical methods for surface interface problems, primarily due to the intricate challenges inherent in handling both the underlying surface and the on-surface interface. Anita Mayo pioneered the approach of embedding irregular domains into a regular Cartesian grid, combining boundary integral equations with fast Poisson solvers to achieve highly accurate numerical solutions [35,36]. Subsequently, Mayo and Greenbaum extended this framework by coupling Mayo's integral equation–finite difference method with Greenbaum's iterative algorithms to efficiently solve the dense, nonsymmetric linear systems arising from such discretizations on irregular domains [37]. The local tangential lifting method mitigates this issue by discretizing the surface PDE via a lifting process onto the tangent plane and utilizing an immersed boundary approach with a regularized delta function to solve the moving interface problem on surfaces [38]. Furthermore, there has been a concerted effort to adapt the immersed finite element method for surface interface problems [39–41].

The boundary integral method has demonstrated success in solving interface problems, attributed to its high efficiency through dimension reduction and superior accuracy. Nonetheless, in the context of a curved two-dimensional manifold, which results in variable coefficients, the absence of a closed-form Green's function renders the conventional boundary integral method ineffective. Among the recent literature, notable contributions include Goodwill and O'Neil's parametrix method [42] and Kropinski et al.'s FMM-accelerated Laplace-Beltrami solver [43,44].

The key advantage of the KFBI method lies in its generalization of traditional boundary integral equation (BIE) frameworks while avoiding their inherent limitations. For example, in interface problems with discontinuous coefficients, the KFBI approach naturally enforces jump conditions via implicit boundary integrals, bypassing the cumbersome layer-potential evaluations required by classical methods. Furthermore, its compatibility with standard PDE discretizations (e.g., finite differences or finite volumes) enables seamless integration into existing computational workflows.

This work extends the KFBI methodology to elliptic PDEs on curved surfaces, emphasizing its capability to handle both boundary value and interface problems with unmatched simplicity and robustness. Numerical experiments validate the method's performance against analytical solutions and benchmark problems, underscoring its potential as a versatile tool for surface PDE simulations.

This paper is organized as follows: Section 2 provides preliminary results on the geometry of embedding surfaces and formulates the surface elliptic PDE problems, including the boundary value problems and the interface problems. Section 3 introduces the boundary integral formulations corresponding to various surface PDEs. Based on the boundary integral formulations, kernel-free boundary integral methods for solving surface boundary value problems and interface problems are proposed in Section 4. The algorithms are summarized in Section 5. Extensive numerical experiments are reported in Section 6, demonstrating the accuracy and efficiency of the proposed methods. Finally, some conclusions are drawn in Section 7.

## 2. Elliptic PDEs on surfaces

### 2.1. Geometry of embedding surfaces

As illustrated in Fig. 1, consider a smooth 2-dimensional Riemannian manifold $\mathcal{S} \subset \mathbb{R}^3$, which can be closed or open. Suppose $\mathcal{S}$ has a regular parameterization $\boldsymbol{X}(\boldsymbol{\xi})$, where $\boldsymbol{\xi} = (\xi_1, \xi_2) \in \mathbb{R}^2$ and $\boldsymbol{X} : \mathbb{R}^2 \to \mathbb{R}^3$ is the embedding map. We denote by $\Omega \subset \mathbb{R}^2$ the preimage of $\mathcal{S}$, and assume, without loss of generality, that $\Omega$ is a planar rectangular domain. Let $\Gamma = \boldsymbol{X}(\gamma)$ be a closed smooth curve on $\mathcal{S}$, where $\gamma \subset \Omega$ is a simple closed curve defined by $\boldsymbol{r}(s) = (r_1(s), r_2(s))^T$ with $0 < s < |\gamma|$ being the arc-length parameter. Suppose $\gamma$ separates $\Omega$ into the interior region $\Omega^+$ and the exterior region $\Omega^-$ whose images under $\boldsymbol{X}$ are $\mathcal{S}^+$ and $\mathcal{S}^-$, such that $\Gamma = \mathcal{S}^+ \cap \mathcal{S}^-$.

Denote $\partial_i := \partial_{\xi_i}$ for $i = 1, 2$. The Riemannian metric tensor $\mathbf{g} = (g_{ij})$ on $\mathcal{S}$ can be defined as

$$g_{ij} := \partial_i \boldsymbol{X} \cdot \partial_j \boldsymbol{X}, \qquad g := \det \mathbf{g}, \qquad g^{ij} := (\mathbf{g}^{-1})_{ij}, \qquad i, j = 1, 2. \tag{2.1}$$

Let $\boldsymbol{e}$ denote the unit tangent vector of $\Gamma$, $\boldsymbol{n}$ the normal vector of $\mathcal{S}$, and let $\boldsymbol{\nu}$ be the outer conormal vector, which is considered tangent to $\mathcal{S}$ and normal to $\Gamma$, i.e.

$$\boldsymbol{e} = \partial_s(\boldsymbol{X} \circ \boldsymbol{r}) = \sum_{i=1}^{2} \partial_s r_i \partial_i \boldsymbol{X}, \qquad \boldsymbol{n} = \frac{\partial_1 \boldsymbol{X} \times \partial_2 \boldsymbol{X}}{|\partial_1 \boldsymbol{X} \times \partial_2 \boldsymbol{X}|}, \qquad \boldsymbol{\nu} = \boldsymbol{e} \times \boldsymbol{n}. \tag{2.2}$$

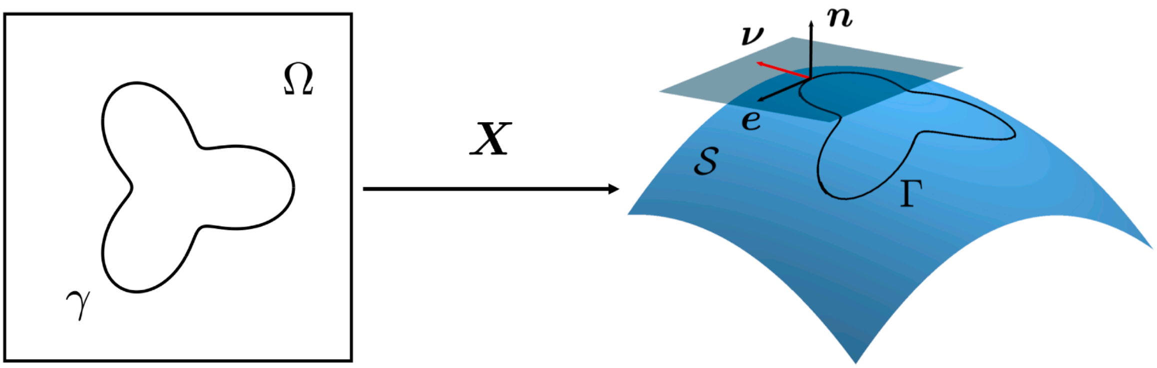

**Fig. 1.** A schematic illustration of a parametric surface and an irregular domain defined on it.

The differential operators with respect to $\mathcal{S}$ are defined as follows:

$$\nabla_{\mathcal{S}} f := \sum_{1\le i,j\le 2} g^{ij}\partial_i f \partial_j \boldsymbol{X}, \qquad \nabla_{\mathcal{S}}\cdot \boldsymbol{f} := \mathrm{Tr}(\nabla_{\mathcal{S}}\boldsymbol{f}) = \sum_{i=1}^{2}\frac{1}{\sqrt{g}}\partial_i(\sqrt{g}f_i), \tag{2.3}$$

where $\boldsymbol{f} = f_1\partial_1\boldsymbol{X} + f_2\partial_2\boldsymbol{X}$. Consequently, the Laplace-Beltrami operator $\Delta_{\mathcal{S}}$ (also termed the surface Laplacian) on $\mathcal{S}$ is given by

$$\Delta_{\mathcal{S}} f := \nabla_{\mathcal{S}}\cdot\nabla_{\mathcal{S}} f = \sum_{1\le i,j\le 2}\frac{1}{\sqrt{g}}\partial_i\left(\sqrt{g}g^{ij}\partial_j f\right). \tag{2.4}$$

Given a piecewise $C^1$ function $f : \mathcal{S}\to\mathbb{R}$, we define the jump of $f$ and its normal derivative across the interface at $\boldsymbol{p}\in\Gamma$. To this end, consider a curve $\boldsymbol{y}(s)$ on $\mathcal{S}$ such that $\boldsymbol{y}(0)=\boldsymbol{p}$ and $\boldsymbol{y}'(0)=\boldsymbol{\nu}(\boldsymbol{p})$, where $\boldsymbol{\nu}$ is the conormal vector. The jump of $f$ and its normal derivative are then defined as follows:

$$[f](\boldsymbol{p}) = f|_{\Gamma_+}(\boldsymbol{p}) - f|_{\Gamma_-}(\boldsymbol{p}) := \lim_{\varepsilon\to 0^+}(f\circ\boldsymbol{y})(-\varepsilon) - (f\circ\boldsymbol{y})(\varepsilon), \tag{2.5a}$$

$$\begin{aligned}\left[\boldsymbol{\nu}\cdot\nabla_{\mathcal{S}} f\right](\boldsymbol{p}) &= \boldsymbol{\nu}\cdot\nabla_{\mathcal{S}} f|_{\Gamma_+}(\boldsymbol{p}) - \boldsymbol{\nu}\cdot\nabla_{\mathcal{S}} f|_{\Gamma_-}(\boldsymbol{p})\\ &:= \lim_{\varepsilon\to 0^+}\boldsymbol{\nu}\cdot((\nabla_{\mathcal{S}} f\circ\boldsymbol{y})(-\varepsilon) - (\nabla_{\mathcal{S}} f\circ\boldsymbol{y})(\varepsilon)).\end{aligned} \tag{2.5b}$$

**Lemma 2.1** (Divergence theorem, [45]). *Let $\mathcal{S}$ be a compact orientable $C^2$-hypersurface with normal vector field $\mathbf{n}$, let $\boldsymbol{f}\in[C^1(\mathcal{S})]^3$. Then it holds that*

$$\int_{\mathcal{S}} \nabla_{\mathcal{S}}\cdot\boldsymbol{f} + H\boldsymbol{f}\cdot\boldsymbol{n}\,\mathrm{d}\mu = \int_{\partial\mathcal{S}}\boldsymbol{f}\cdot\boldsymbol{\nu}\,\mathrm{d}s, \tag{2.6}$$

*where $\mu$ is the Riemannian measure on $\mathcal{S}$, $H$ denotes the mean curvature and $\mathbf{v}$ represents the outer unit conormal to $\partial\mathcal{S}$.*

**Lemma 2.2** (Green's identity, [45]). *Suppose $f\in C^2(\mathcal{S}), g\in C^1(\mathcal{S})$, then*

$$\int_{\mathcal{S}} g\Delta_{\mathcal{S}} f + \nabla_{\mathcal{S}} f\cdot\nabla_{\mathcal{S}} g\,\mathrm{d}\mu = \int_{\partial\mathcal{S}} g\nabla_{\mathcal{S}} f\cdot\boldsymbol{\nu}\,\mathrm{d}s. \tag{2.7}$$

### 2.2. Boundary value problem

We consider boundary value problems on an open surface $\mathcal{S}^+$ with a smooth boundary $\partial\mathcal{S}^+$. Let $\kappa\ge 0$ be a constant coefficient. Given the function $f : \mathcal{S}^+\to\mathbb{R}$, the boundary value problem for an elliptic PDE is formulated as finding a solution $u : \mathcal{S}^+\to\mathbb{R}$ such that

$$\Delta_{\mathcal{S}} u - \kappa u = f, \qquad \text{in } \mathcal{S}^+, \tag{2.8}$$

subject to either the Dirichlet boundary condition

$$u = g_D, \qquad \text{on } \partial\mathcal{S}^+, \tag{2.9}$$

or the Neumann boundary condition

$$\boldsymbol{\nu}\cdot\nabla_{\mathcal{S}} u = g_N, \qquad \text{on } \partial\mathcal{S}^+. \tag{2.10}$$

Here, $g_D$ and $g_N$ are the Dirichlet and Neumann boundary data, respectively. The Dirichlet problem admits a unique solution for all $\kappa\ge 0$, whereas the Neumann problem is uniquely solvable only when $\kappa > 0$. If $\kappa = 0$, as a direct result of the Fredholm Alternative, the Neumann data $g_N$ must satisfy the compatibility condition

$$\int_{\mathcal{S}^+} f\,\mathrm{d}\mu = \int_{\partial\mathcal{S}^+} g_N\,\mathrm{d}s, \tag{2.11}$$

in which case the solution is determined only up to an additive constant.

### 2.3. Interface problem

Now we consider the elliptic interface problem defined on a given surface $\mathcal{S}$. Let $\beta(\boldsymbol{p})$ and $\kappa(\boldsymbol{p})$ be piecewise constant diffusion and reaction coefficients, with $\beta \equiv \beta^{\pm} > 0$ and $\kappa \equiv \kappa^{\pm} \geq 0$ in $\mathcal{S}^{\pm}$. For an open surface, we further assume that the internal interface $\Gamma$ lies away from the boundary $\partial\mathcal{S}$; that is, $\mathrm{dist}(\Gamma, \partial\mathcal{S}) > 0$. Suppose $f$ is a piecewise smooth function on $\mathcal{S}$. Then the elliptic interface problem for the solution $u$ is formulated as follows:

$$\nabla_{\mathcal{S}} \cdot \left(\beta \nabla_{\mathcal{S}} u\right) - \kappa u = f, \qquad \text{in } \mathcal{S} \setminus \Gamma, \tag{2.12}$$

subject to interface conditions

$$[u] = g_1, \qquad \text{on } \Gamma, \tag{2.13a}$$

$$\left[\beta \boldsymbol{v} \cdot \nabla_{\mathcal{S}} u\right] = g_2, \qquad \text{on } \Gamma, \tag{2.13b}$$

where $g_1$ and $g_2$ are two given functions defined on $\Gamma$. If $\mathcal{S}$ is open, an additional boundary condition must be imposed on $\partial\mathcal{S}$. For example, the Dirichlet boundary condition

$$u = g_0 \qquad \text{on } \partial\mathcal{S}, \tag{2.14}$$

where $g_0$ is the prescribed boundary data. If $\mathcal{S}$ is closed (and hence has no boundary), then when $\kappa \equiv 0$ the problem has a nontrivial nullspace. Therefore, in such cases we assume that either $\kappa^{+} \neq 0$ or $\kappa^{-} \neq 0$, so that the problem admits a unique solution.

## 3. Boundary integral formulations

The boundary value and interface problems described in the previous section are reformulated as boundary integral equations in this section.

### 3.1. Integral operators

Let $\boldsymbol{p}$ and $\boldsymbol{q}$ be points in $\mathcal{S}$. Let $\delta(\cdot)$ be the surface Dirac delta function, defined as a distribution on $\mathcal{S}$ satisfying

$$\int_{\mathcal{S}} \phi(\boldsymbol{q})\, \delta(\boldsymbol{p} - \boldsymbol{q})\, \mathrm{d}\mu = \phi(\boldsymbol{p}), \qquad \forall\, \phi \in C_c^{\infty}(\mathcal{S}), \tag{3.1}$$

where $C_c^{\infty}(\mathcal{S})$ represents the space of smooth functions with compact support. We define the Green's function $G(\boldsymbol{p}, \boldsymbol{q})$ on $\mathcal{S}$ with respect to the elliptic operator $\Delta_{\mathcal{S}} - \kappa$ by

$$(\Delta_{\mathcal{S},\boldsymbol{q}} - \kappa)\, G(\boldsymbol{p}, \boldsymbol{q}) = \delta(\boldsymbol{p} - \boldsymbol{q}), \qquad \boldsymbol{q} \in \mathcal{S}, \tag{3.2}$$

where $\Delta_{\mathcal{S},\boldsymbol{q}}$ is the Laplace-Beltrami operator acting on the $\boldsymbol{q}$-variable. For an open surface $\mathcal{S}$, the following homogeneous boundary condition is imposed to guarantee its existence and uniqueness:

$$G(\boldsymbol{p}, \boldsymbol{q}) = 0, \qquad \boldsymbol{q} \in \partial\mathcal{S}. \tag{3.3}$$

The Laplace-Beltrami operator can be viewed as a variable-coefficient elliptic differential operator. In certain special geometries, such as the sphere, one can write down the Green's function explicitly [44]. However, for a generic smooth surface, no closed-form expression is available. Rather than resorting to parametrix or Levi-function constructions [42,46], which trade off the general utility of the Green's function for analytic formulas, we rely solely on the layer-potential framework built from the Green's function's abstract properties, without requiring its explicit form.

For a point $\boldsymbol{p} \in \mathcal{S}$, we define the following potential functions,

$$\text{Volume potential}: \ (Vf)(\boldsymbol{p}) := \int_{\mathcal{S}} f(\boldsymbol{q}) G(\boldsymbol{p}, \boldsymbol{q})\, \mathrm{d}\mu_{\boldsymbol{q}}, \tag{3.4a}$$

$$\text{Single-layer potential}: \ (S\psi)(\boldsymbol{p}) := \int_{\Gamma} \psi(\boldsymbol{q}) G(\boldsymbol{p}, \boldsymbol{q})\, \mathrm{d}s_{\boldsymbol{q}}, \tag{3.4b}$$

$$\text{Double-layer potential}: \ (D\varphi)(\boldsymbol{p}) := \int_{\Gamma} \varphi(\boldsymbol{q}) \boldsymbol{v}(\boldsymbol{q}) \cdot \nabla_{\mathcal{S},\boldsymbol{q}} G(\boldsymbol{p}, \boldsymbol{q})\, \mathrm{d}s_{\boldsymbol{q}}. \tag{3.4c}$$

For $\boldsymbol{p} \in \mathcal{S} \setminus \Gamma$, the integrands are smooth, so the corresponding potentials are finite and smooth on $\mathcal{S} \setminus \Gamma$. Moreover, applying the differential operator $\Delta_{\mathcal{S}} - \kappa$ to the potential functions (3.4) yields

$$(\Delta_{\mathcal{S}} - \kappa)\, Vf = f, \qquad (\Delta_{\mathcal{S}} - \kappa)\, S\psi = 0, \qquad (\Delta_{\mathcal{S}} - \kappa)\, D\varphi = 0, \qquad \text{in } \mathcal{S} \backslash \Gamma. \tag{3.5}$$

For $\boldsymbol{p} \in \Gamma$, both $Vf$ and $S\psi$ are continuous at $\boldsymbol{p}$. Hence, traces of $Vf$ and $S\psi$ on $\Gamma$ are denoted using the same notation for simplicity. Since the integral $D\varphi$ on $\Gamma$ is divergent, we interpret it as a principal value integral and denote it by $K\varphi$, i.e.

$$(K\varphi)(\boldsymbol{p}) := \text{p.v.} \int_{\Gamma} \varphi(\boldsymbol{q}) \boldsymbol{v}(\boldsymbol{q}) \cdot \nabla_{\mathcal{S},\boldsymbol{q}} G(\boldsymbol{p}, \boldsymbol{q})\, \mathrm{d}s_{\boldsymbol{q}} = \frac{1}{2}((D\varphi)|_{\Gamma_+} + (D\varphi)|_{\Gamma_-})(\boldsymbol{p}). \tag{3.6}$$

Correspondingly, the double-layer potential is discontinuous on $\Gamma$ and satisfies the following jump relation,

$$(D\varphi)|_{\Gamma^+}(\boldsymbol{p}) - (D\varphi)|_{\Gamma^-}(\boldsymbol{p}) = \varphi(\boldsymbol{p}). \tag{3.7}$$

The normal derivative of $D\varphi$ is also continuous across $\Gamma$.

The normal derivative of $Vf$ remains continuous across $\Gamma$, whereas the normal derivative of the single-layer potential satisfies the following jump relation

$$\boldsymbol{\nu}\cdot\nabla_{\mathcal{S}}(\mathcal{S}\psi)|_{\Gamma^+}(\boldsymbol{p}) - \boldsymbol{\nu}\cdot\nabla_{\mathcal{S}}(\mathcal{S}\psi)|_{\Gamma^-}(\boldsymbol{p}) = -\psi(\boldsymbol{p}). \tag{3.8}$$

The adjoint double-layer integral is defined by

$$\begin{aligned}(K'\varphi)(\boldsymbol{p}) &:= \text{p.v.}\int_\Gamma \varphi(\boldsymbol{q})\boldsymbol{\nu}(\boldsymbol{p})\cdot\nabla_{\mathcal{S},\boldsymbol{p}}G(\boldsymbol{p},\boldsymbol{q})\,\mathrm{d}s_{\boldsymbol{q}}\\ &= \frac{1}{2}\big(\boldsymbol{\nu}\cdot\nabla_{\mathcal{S}}(\mathcal{S}\psi)|_{\Gamma^+} + \boldsymbol{\nu}\cdot\nabla_{\mathcal{S}}(\mathcal{S}\psi)|_{\Gamma^-}\big)(\boldsymbol{p}).\end{aligned} \tag{3.9}$$

and its normal derivative is also continuous. The hyper-singular integral operator is defined as follows

$$(H\varphi)(\boldsymbol{p}) := \text{f.p.}\int_\Gamma \boldsymbol{\nu}^T(\boldsymbol{p})\big(\nabla_{\mathcal{S},\boldsymbol{p}}\nabla_{\mathcal{S},\boldsymbol{q}}G(\boldsymbol{p},\boldsymbol{q})\big)\boldsymbol{\nu}(\boldsymbol{q})\varphi(\boldsymbol{q})\,\mathrm{d}s_{\boldsymbol{q}}, \tag{3.10}$$

where the notation f.p. means the Hadamard finite part integral.

For a detailed discussion of the above integral operators and their associated jump relations, we refer the reader to [47,48].

### 3.2. Boundary value problem

Analogous to the planar case in [30], the solution $u(\boldsymbol{p})$ to the Dirichlet BVP (2.8)–(2.9) can be expressed as a sum of a volume potential and a double-layer potential:

$$u(\boldsymbol{p}) = Vf(\boldsymbol{p}) + D\varphi(\boldsymbol{p}), \qquad \text{in } \mathcal{S}, \tag{3.11}$$

where the density $\varphi(\boldsymbol{p})$ satisfies a Fredholm boundary integral equation (BIE) of the second kind as follows:

$$\frac{1}{2}\varphi(\boldsymbol{p}) + K\varphi(\boldsymbol{p}) + Vf(\boldsymbol{p}) = g_D(\boldsymbol{p}), \qquad \text{on } \Gamma. \tag{3.12}$$

The derivation follows an approach similar to that in [31] by applying the Green's identities (2.6)–(2.7). Details are omitted here for brevity.

Similarly, the solution to the Neumann BVP (2.8)&(2.10) can be expressed in terms of a volume potential and a single-layer potential:

$$u(\boldsymbol{p}) = Vf(\boldsymbol{p}) - \mathcal{S}\psi(\boldsymbol{p}), \qquad \text{in } \mathcal{S}. \tag{3.13}$$

The density function $\psi(\boldsymbol{p})$ is required to satisfy the following BIE:

$$\frac{1}{2}\psi(\boldsymbol{p}) - K'\psi(\boldsymbol{p}) + \boldsymbol{\nu}\cdot\nabla_{\mathcal{S}}(Vf)(\boldsymbol{p}) = g_N(\boldsymbol{p}), \qquad \text{on } \Gamma. \tag{3.14}$$

Since the Green's function can be viewed as a perturbation of the Green's function in Euclidean space by a more regular term, the operators $K$ and $K'$ remain compact, with spectra clustered around zero [49]. Consequently, the operators $\frac{1}{2}\mathcal{I}+K$ and $\frac{1}{2}\mathcal{I}-K'$ have spectra clustered around $1/2$, which is away from zero. This spectral property enables the use of Krylov subspace iterative methods, such as GMRES, to efficiently solve the resulting discrete linear system, provided the discrete operators exhibit similar spectral behavior.

### 3.3. Interface problem

For the generic case when $\kappa^+/\beta^+ \neq \kappa^-/\beta^-$, the Green's functions associated with the differential operators in $\mathcal{S}^+$ and $\mathcal{S}^-$ must be defined separately. Let $G^\pm(\boldsymbol{p},\boldsymbol{q})$ be the Green's function associated with the interface problem with variable coefficient in $\mathcal{S}^\pm$, which satisfies

$$\left(\Delta_{\mathcal{S},\boldsymbol{q}} - \frac{\kappa^\pm}{\beta^\pm}\right)G^\pm(\boldsymbol{p},\boldsymbol{q}) = \delta(\boldsymbol{p}-\boldsymbol{q}), \qquad \boldsymbol{q}\in\mathcal{S}^\pm. \tag{3.15}$$

Similar to the previous work [31], the single-layer, double-layer, adjoint double-layer, and hyper-singular boundary integrals need to be defined for both the interior and exterior regions. We denote the associated integral operators as $V^\pm, K^\pm, \mathcal{S}^\pm, (K')^\pm, H^\pm$.

Let $\varphi = u^+, \psi = \boldsymbol{\nu}\cdot\nabla_{\mathcal{S}}u^-$ be two unknown density functions. Applying the interface conditions (2.13), we can derive the following system of equations:

$$\frac{1}{2}\varphi = K^+\varphi - \mathcal{S}^+\psi - \mathcal{S}^+g_N + V^+f^+, \tag{3.16a}$$

$$\frac{1}{2}(\varphi - g_D) = -K^-\varphi + \mathcal{S}^-\psi + K^-g_D + V^-f^-, \tag{3.16b}$$

$$\frac{1}{2}(\psi + g_N) = H^+\varphi - (K')^+\psi - (K')^+g_N + \beta^+\boldsymbol{\nu}\cdot\nabla_{\mathcal{S}}V^+f^+, \tag{3.16c}$$

$$\frac{1}{2}\psi = -H^-\psi + (K')^-\psi + H^- g_D + \beta^- \boldsymbol{v}\cdot\nabla_{\mathcal{S}} V^- f^-. \tag{3.16d}$$

Adding (3.16a) to (3.16b), (3.16c) to (3.16d), and rearranging the terms, the interface problem is reformulated as a system of two Fredholm integral equations of the second kind: for $\boldsymbol{q}\in\mathcal{S}$,

$$\varphi - \left(D^+ - D^-\right)\varphi + \left(S^+ - S^-\right)\psi = r(\mathbf{q}), \tag{3.17a}$$

$$-\left(H^+ - H^-\right)\varphi + \psi + \left((K')^+ - (K')^-\right)\psi = s(\mathbf{q}), \tag{3.17b}$$

where $r, s$ are given by

$$r(\mathbf{q}) := \frac{1}{2} g_D + V^+ f^+ + V^- f^- - S^+ g_N + D^- g_D, \tag{3.18a}$$

$$s(\mathbf{q}) := -\frac{1}{2} g_N + \beta^+ \boldsymbol{v}\cdot\nabla_{\mathcal{S}} V^+ f^+ + \beta^- \boldsymbol{v}\cdot\nabla_{\mathcal{S}} V^- f^- - (K')^+ g_N + H^- g_D. \tag{3.18b}$$

After solving the boundary integral equation system to determine $\varphi$ and $\psi$, the solutions $u^+$ and $u^-$ are then obtained by evaluating the following integrals:

$$u^+(\boldsymbol{p}) = D^+\varphi - S^+\psi - S^+ g_N + V^+ f^+, \tag{3.19a}$$

$$u^-(\boldsymbol{p}) = -D^-\varphi + S^-\psi + S^- g_N + V^- f^-. \tag{3.19b}$$

In the special case when $\kappa^+/\beta^+ = \kappa^-/\beta^-$, one can derive a simple boundary integral equation of the second kind with one unknown density function. To this end, we define the following Green's function:

$$\left(\Delta_{\mathcal{S},q} - \frac{\kappa^\pm}{\beta^\pm}\right) G(\boldsymbol{p},\boldsymbol{q}) = \delta(\boldsymbol{p}-\boldsymbol{q}), \qquad \boldsymbol{q}\in\mathcal{S}. \tag{3.20}$$

Let $\psi$ be an unknown single-layer density. In a manner similar to [31], one can express the solution as a linear combination of the single-layer, double-layer and volume potential, i.e.

$$u(\boldsymbol{p}) = D g_1(\boldsymbol{p}) - S\psi(\boldsymbol{p}) + V\hat{f}(\boldsymbol{p}), \qquad \hat{f}(\boldsymbol{p}) := f(\boldsymbol{p})/\beta(\boldsymbol{p}), \qquad \boldsymbol{p}\in\mathcal{S}. \tag{3.21}$$

One can easily verify that the above representation satisfies the PDE (2.12), the interface condition (2.13a), and the jump condition $\left[\boldsymbol{v}\cdot\nabla_{\mathcal{S}} u\right] = \psi$. As long as $u$ also satisfies the interface condition (2.13b), it will serve as a solution to the interface problem (2.12)–(2.13).

By taking the derivative of $u$ in the conormal direction, we obtain

$$H g_1 - K'\psi + \boldsymbol{v}\cdot\nabla_{\mathcal{S}}(V\hat{f}) = \boldsymbol{v}\cdot\nabla_{\mathcal{S}} u|_{\Gamma^+} - \frac{1}{2}\psi = \boldsymbol{v}\cdot\nabla_{\mathcal{S}} u|_{\Gamma^-} + \frac{1}{2}\psi, \qquad \boldsymbol{p}\in\Gamma. \tag{3.22}$$

Applying the interface condition (2.13b) results in a boundary integral equation of the second kind for the density $\psi$:

$$\psi - 2A_\beta K'\psi = \frac{2}{\beta^+ + \beta^-} g_2 - 2A_\beta\left(H g_1 + \boldsymbol{v}\cdot\nabla_{\mathcal{S}}(V\hat{f})\right) := \hat{g}_2, \qquad \text{on } \Gamma, \tag{3.23}$$

where $A_\beta = (\beta^+ - \beta^-)/(\beta^+ + \beta^-) \in (-1,1)$ is the Atwood ratio. For $\beta^\pm \neq 0$, the integral equation above with a homogeneous right-hand side admits only the zero solution. Hence, by the Fredholm Alternative, the boundary integral Eq. (3.23) is uniquely solvable and has a bounded inverse.

## 4. Kernel-free boundary integral method

In this section, we introduce the kernel-free boundary integral method for evaluating boundary and volume integrals by solving equivalent interface problems on a Cartesian grid with a finite difference method.

### 4.1. Equivalent interface problems

Rather than interpreting the volume potential, the single-layer potential, and the double-layer potential through their integral representations, we regard them as solutions of simpler interface problems, with their jump relations given in Section 3.1.

The interface problems corresponding to the three potentials $Vf$, $S\psi$, and $D\varphi$ can be unified in the following form,

$$\Delta_{\mathcal{S}} u - \kappa u = F, \qquad \text{in } \mathcal{S}\setminus\Gamma, \tag{4.1a}$$

$$[u] = \Phi, \qquad \text{on } \Gamma, \tag{4.1b}$$

$$\left[\boldsymbol{v}\cdot\nabla_{\mathcal{S}} u\right] = \Psi, \qquad \text{on } \Gamma, \tag{4.1c}$$

where the source term $F$ and jump data $\Phi$, $\Psi$ are specified as follows,

- $u = Vf$: $F = f$, $\Phi = 0$, $\Psi = 0$;
- $u = S\psi$: $F = 0$, $\Phi = 0$, $\Psi = -\psi$;
- $u = D\varphi$: $F = 0$, $\Phi = \varphi$, $\Psi = 0$.

These interface problems are significantly simpler than the boundary value problem (2.8) and the original interface problem (2.12), as they involve constant coefficients and known density functions. This enables the construction of numerical schemes that require only right-hand side corrections and can be efficiently solved using fast elliptic solvers. As a result, one no longer needs an explicit analytical expression for the Green's function to perform numerical quadrature, and (nearly) singular integrals can be completely avoided.

For numerical convenience, we pull back functions on $\mathcal{S}$ to the planar domain $\Omega$. For a surface function $f : \mathcal{S} \to \mathbb{R}$, we denote its pullback under the parametrization $\boldsymbol{X}$ by $\widetilde{f} = f \circ \boldsymbol{X}$. Then the interface problem (4.1) can be reformulated as an interface problem on a planar domain with variable coefficients

$$\sum_{i,j=1}^{2} \partial_i\big(a_{ij}(\boldsymbol{x})\partial_j \widetilde{u}\big)(\boldsymbol{x}) - a(\boldsymbol{x})\widetilde{u}(\boldsymbol{x}) = \widetilde{f}(\boldsymbol{x}), \qquad \text{in } \Omega \setminus \gamma, \tag{4.2a}$$

$$[\widetilde{u}](\boldsymbol{x}) = \widetilde{\Phi(\boldsymbol{x})}, \qquad \text{on } \gamma, \tag{4.2b}$$

$$\sum_{i,j=1}^{2} \beta_{ij}(\boldsymbol{x})\big[\partial_i \widetilde{u}\big](\boldsymbol{x}) = \widetilde{\Psi(\boldsymbol{x})}, \qquad \text{on } \gamma. \tag{4.2c}$$

where the spatially dependent functions are given by

$$a = \kappa\sqrt{g}, \qquad \beta_{ij} = g^{ij}\big(\widetilde{\boldsymbol{\nu}} \cdot \partial_j \boldsymbol{X}\big), \qquad a_{ij} = \sqrt{g}g^{ij}, \qquad f = \sqrt{g}F. \tag{4.3}$$

### 4.2. *Corrected finite difference scheme*

A finite difference scheme is devised for solving the interface problem (4.2), with right-hand side correction to incorporate the jump of the solution at the interface. Consider a variable coefficient self-adjoint differential operator $L$, defined as

$$L = \sum_{i,j=1}^{2} \frac{\partial}{\partial x_i}\left(a_{ij}(\boldsymbol{x})\frac{\partial}{\partial x_j}\right) - a(\boldsymbol{x}), \qquad a_{ij}(\boldsymbol{x}) = a_{ji}(\boldsymbol{x}), \qquad \boldsymbol{x} \in \Omega. \tag{4.4}$$

where $a_{ij}, a$ are spatially dependent functions. Assume that $a_{ij} \in C^1(\Omega)$ is pointwise positive definite and $a \geq 0$ such that the differential operator $L$ is negative definite with a suitable boundary condition on $\partial\Omega$.

For simplicity, we assume that the planar domain $\Omega$ is a square $\Omega = (-1, 1)^2$. Let $N$ be a positive integer. We uniformly partition $\Omega$ into a Cartesian grid in each spatial direction with grid spacing $h = \frac{2}{N}$. The set of grid nodes is denoted by $\overline{\Omega_h}$, defined as

$$\overline{\Omega_h} = \big\{(x_i, y_j) = (-1 + ih, -1 + jh) \mid i, j = 0, 1, \cdots, N\big\}. \tag{4.5}$$

The sets of interior grid nodes $\Omega_h$ and boundary grid nodes $\partial\Omega_h$ are defined as

$$\Omega_h = \big\{(x_i, y_j) = (-1 + ih, -1 + jh) \mid i, j = 1, 2, \cdots, N-1\big\}, \qquad \partial\Omega_h = \overline{\Omega_h}\backslash\Omega_h. \tag{4.6}$$

The diagonal terms $\frac{\partial}{\partial x}a_{11}(x, y)\frac{\partial}{\partial x} + \frac{\partial}{\partial y}a_{22}(x, y)\frac{\partial}{\partial y} - a(x, y)$ at a grid node $\boldsymbol{x} = (x, y) \in \Omega_h$ can be discretized with a standard five-point difference scheme, represented as

$$\begin{aligned} &h^{-2}\begin{bmatrix} 0 & a_{22}(x, y+h/2) & 0 \\ a_{11}(x-h/2, y) & \begin{Bmatrix} -a_{11}(x-h/2, y) - a_{11}(x+h/2, y) \\ -a_{22}(x, y+h/2) - a_{22}(x, y-h/2) \end{Bmatrix} & a_{11}(x+h/2, y) \\ 0 & a_{22}(x, y-h/2) & 0 \end{bmatrix} \\ &- \begin{bmatrix} 0 & 0 & 0 \\ 0 & a(x,y) & 0 \\ 0 & 0 & 0 \end{bmatrix}. \end{aligned} \tag{4.7}$$

The discretization of the mixed term $\frac{\partial}{\partial x}a_{12}(x, y)\frac{\partial}{\partial y} + \frac{\partial}{\partial y}a_{12}(x, y)\frac{\partial}{\partial x}$ results in a seven-point difference scheme, whose stencil depends on the sign of the off-diagonal coefficient $a_{12}$. If $a_{12}(x, y) = a_{21}(x, y) < 0$, the seven-point difference scheme reads

$$\frac{h^{-2}}{2}\begin{bmatrix} -a_{12}^A - a_{12}^B & a_{12}^A + a_{12}^C & 0 \\ a_{12}^B + a_{12}^D & -a_{12}^C - a_{12}^D - a_{12}^E - a_{12}^F & a_{12}^H + a_{12}^F \\ 0 & a_{12}^E + a_{12}^G & -a_{12}^H - a_{12}^G \end{bmatrix}, \tag{4.8}$$

where the upper index indicates the evaluation at $\boldsymbol{x} + \delta h$ with $\delta$ specified below

$$\begin{array}{c|cccccccc} & \text{A} & \text{B} & \text{C} & \text{D} & \text{E} & \text{F} & \text{G} & \text{H} \\ \hline \delta & \left(-\frac{1}{2}, 1\right) & \left(-1, \frac{1}{2}\right) & \left(0, \frac{1}{2}\right) & \left(-\frac{1}{2}, 0\right) & \left(0, -\frac{1}{2}\right) & \left(\frac{1}{2}, 0\right) & \left(\frac{1}{2}, -1\right) & \left(1, -\frac{1}{2}\right). \end{array} \tag{4.9}$$

If $a_{12}(x,y) = a_{21}(x,y) > 0$, then the seven-point difference scheme is given by

$$\frac{h^{-2}}{2}\begin{bmatrix} 0 & -a_{12}^A - a_{12}^C & a_{12}^A + a_{12}^H \\ -a_{12}^B - a_{12}^D & a_{12}^C + a_{12}^D + a_{12}^E + a_{12}^F & -a_{12}^H - a_{12}^F \\ a_{12}^B + a_{12}^G & -a_{12}^E - a_{12}^G & 0 \end{bmatrix} \tag{4.10}$$

where the upper index indicates the evaluation at $\boldsymbol{x} + \delta h$ with $\delta$ specified below:

$$\begin{array}{c|cccccccc} & \text{A} & \text{B} & \text{C} & \text{D} & \text{E} & \text{F} & \text{G} & \text{H} \\ \hline \delta & \left(\frac{1}{2},1\right) & \left(-1,-\frac{1}{2}\right) & \left(0,\frac{1}{2}\right) & \left(-\frac{1}{2},0\right) & \left(0,-\frac{1}{2}\right) & \left(\frac{1}{2},0\right) & \left(-\frac{1}{2},-1\right) & \left(1,\frac{1}{2}\right). \end{array} \tag{4.11}$$

We denote the associated coefficient matrix of the seven-point scheme by $L_h$. The stencil selection procedure according to the off-diagonal coefficient is mainly for ensuring the stability of the matrix $L_h$ and the solvability of the resulting linear system. In particular, under mild assumptions, the seven-point finite difference scheme is second-order and the negative of $L_h$ is an M-matrix with guaranteed invertibility and positivity [50, p. 104]:

**Lemma 4.1** ([50]). *Assume that $a_{ij} \in C^{2,1}(\overline{\Omega})$ and $|a_{12}(x,y)| < \min(|a_{11}(x,y)|, |a_{22}(x,y)|)$, the finite difference scheme (4.7),(4.8), and (4.10) has second-order consistency and for sufficiently small $h$ the associated matrix $-L_h$ is a symmetric and positive-definite M-matrix.*

We apply the seven-point finite difference scheme to the differential equation $Lu = f$ whose solution $u$ is only expected to be piecewise smooth in $\Omega^\pm$. At grid nodes away from the interface where the solution is smooth, the scheme retains its second order consistency. At grid nodes in the vicinity of the interface, the finite difference scheme may be taken across the interface, leading to large local truncation error due to the non-smoothness of the solution. Such an issue can be addressed by incorporating the leading local truncation error in the finite difference scheme as correction terms to the right-hand side, modifying the local truncation error and leaving the coefficient matrix intact.

Let $u_{ij}$ be the numerical approximation of $u\left(x_i, y_j\right)$. We write the seven-point finite difference scheme in a generic form,

$$L_h u_{ij} = \sum_{(x_r,y_s)\in\overline{\Omega_h}} c_{ijrs} u_{rs} = \sum_{(x_r,y_s)\in S_{ij}} c_{ijrs} u_{rs}, \qquad \left(x_i, y_j\right) \in \Omega_h, \tag{4.12}$$

where $c_{ijrs}$ is the coefficient depending on $a_{ij}, a$ and $S_{ij}$ is the set of stencil nodes of the finite difference operator $L_h$ at $(x_i, y_j)$, defined as

$$S_{ij} = \left\{ \left(x_r, y_s\right) \in \overline{\Omega_h} \mid c_{ijrs} \neq 0 \right\}. \tag{4.13}$$

We define the sets of the regular and irregular nodes, denoted by $\mathcal{R}_h, \mathcal{I}_h$,

$$\mathcal{R}_h := \left\{ \left(x_i, y_j\right) \in \Omega_h \mid S_{ij} \cap \Omega^+ = \emptyset \text{ or } S_{ij} \cap \Omega^- = \emptyset \right\}, \qquad \mathcal{I}_h := \Omega_h \backslash \mathcal{R}_h. \tag{4.14}$$

Let $\Omega_\gamma \supset \mathcal{I}_h$ be a narrow band near $\gamma$ with sufficient width to cover all irregular nodes. Suppose the piecewise smooth solution $u$ can be smoothly extended into $\Omega^\mp$ with the restricted values $u|\Omega^\pm$. We denote the extended smooth functions by $u^\pm$, defined in $\Omega^\pm \cup \Omega_\gamma$. Let $C = u^+ - u^-$ be the difference of the two smooth functions in $\Omega_\gamma$, which is referred to as the correction function. The local truncation error of the finite difference scheme at a grid node $(x_i, y_j) \in \Omega_h$ is given by

$$E_{ij} = L_h u\left(x_i, y_j\right) - f\left(x_i, y_j\right) = D(x_i, y_j; C) + \mathcal{O}(h^2). \tag{4.15}$$

where the leading term $D(x_i, y_j; C)$ is given by

$$D(x_i, y_j; C) = \begin{cases} 0, & \left(x_i, y_j\right) \in \mathcal{R}_h, \\ -\displaystyle\sum_{(x_r,y_s)\in S_{ij}\cap\Omega^-} c_{ijrs} C\left(x_r, y_s\right), & \left(x_i, y_j\right) \in \mathcal{I}_h \cap \Omega^+, \\ \displaystyle\sum_{(x_r,y_s)\in S_{ij}\cap\Omega^+} c_{ijrs} C\left(x_r, y_s\right), & \left(x_i, y_j\right) \in \mathcal{I}_h \cap \Omega^-. \end{cases} \tag{4.16}$$

Since the coefficient satisfies $c_{ijrs} = \mathcal{O}(h^{-2})$, the local truncation error at irregular nodes behaves like $E_{ij} = \mathcal{O}(h^{-2})$. An immediate remedy is to use the value of $D(x_i, y_j; C)$ as correction terms to design a corrected scheme.

Since $D(x_i, y_j; C)$ is a linear combination of the correction function $C$, which is generally not known explicitly but can be approximated by a numerical solution $C_h$, we introduce $\mathcal{Z}_h$ as the set of grid nodes where the correction function is used, i.e.

$$\mathcal{Z}_h = \left( \bigcup_{(x_i,y_j)\in\mathcal{I}_h\cap\Omega^+} \left(S_{ij} \cap \Omega^-\right) \right) \bigcup \left( \bigcup_{(x_i,y_j)\in\mathcal{I}_h\cap\Omega^-} \left(S_{ij} \cap \Omega^+\right) \right). \tag{4.17}$$

Suppose the numerical solution $C_h$ has pointwise third-order accuracy, i.e., $|C - C_h|\left(x_i, y_j\right) = \mathcal{O}(h^3)$ for $\left(x_i, y_j\right) \in \mathcal{Z}_h$. Then the corrected scheme is given by

$$L_h u_{ij} = f\left(x_i, y_j\right) + D(x_i, y_j; C_h), \qquad \left(x_i, y_j\right) \in \Omega_h. \tag{4.18}$$

After correction, the local truncation error is modified to

$$\begin{aligned}\widetilde{E}_{ij} &= L_h u(x_i, y_j) - f(x_i, y_j) - D(x_i, y_j; C_h) \\ &= E_{ij} - D(x_i, y_j; C_h) = \begin{cases} \mathcal{O}(h^2), & (x_i, y_j) \in \mathcal{R}_h, \\ \mathcal{O}(h), & (x_i, y_j) \in \mathcal{I}_h. \end{cases}\end{aligned} \tag{4.19}$$

Since irregular nodes only appear in the vicinity of the interface, which is a co-dimension one object, the first-order local truncation error at irregular nodes is sufficient to result in a uniformly second-order accuracy. As an immediate consequence of Theorem 2.1 in [51], the numerical solution satisfies the following error estimate.

**Theorem 4.2.** *Suppose the local truncation error satisfies $|\widetilde{E}_{ij}| \le ch$ for $(x_i, y_j) \in \mathcal{I}_h$ and $|\widetilde{E}_{ij}| \le ch^2$ for $(x_i, y_j) \in \mathcal{R}_h$. Then we have the error estimate,*

$$|u(x_i, y_j) - u_{ij}| \le ch^2, \qquad (x_i, y_j) \in \Omega_h, \tag{4.20}$$

*where $c$ is dependent on $u$ but independent of $h$.*

The corrected finite-difference scheme leaves the coefficient matrix intact, which permits the use of fast elliptic solvers for the resulting linear system. In particular, exploiting the nested structure of the Cartesian grid, we employ a geometric multigrid solver with a full-multigrid cycle [52], achieving optimal complexity $\mathcal{O}\big(N^2 \log(1/\varepsilon)\big)$, where $\varepsilon$ is the prescribed tolerance and $N^2$ is the total number of grid nodes.

After solving the interface problem, we obtain the grid values of the potential functions. However, in solving boundary integral equations, one would need the boundary integrals on the interface, which are either the trace or normal derivatives of the potential functions on the interface. We apply Lagrange interpolation to extract boundary information from the grid values to complete the integral evaluation on the interface. Since potential functions are not smooth on the interface, corrections are also needed to obtain accurate interpolation. We refer the reader to [30,32] for details of interpolation with the correction function.

### *4.3. Local Cauchy problem*

Here we introduce a numerical approach to obtain the correction function $C_h$. The smooth extension of $f$ is not unique; here we adopt the approach of extending the original PDE. Suppose the piece-wise smooth right-hand side function $f$ can be smoothly extended into $\Omega_\gamma$ from each side to give two smooth functions $f^+$ and $f^-$. The extension of $u$ is done by letting $u^\pm$ be solutions to the equation $Lu^\pm = f^\pm$ in the domain $\Omega^\pm \cap \Omega_\gamma$. By elliptic regularity theory, $u^\pm$ and their difference, the correction function, are expected to be smooth. Denote by $\bar{f} = f^+ - f^-$. A direct computation confirms that the correction function satisfies the Cauchy problem of an elliptic PDE as follows

$$\sum_{i,j=1}^{2} \partial_i\big(a_{ij}\partial_j C\big) - aC = \bar{f}, \qquad \text{in } \Omega_\gamma, \tag{4.21a}$$

$$C = \bar{\Phi}, \qquad \text{on } \gamma, \tag{4.21b}$$

$$\sum_{i,j=1}^{2} \beta_{ij}\partial_i C = \bar{\Psi}, \qquad \text{on } \gamma. \tag{4.21c}$$

where $\bar{\Phi}, \bar{\Psi}$ are smooth Cauchy data given on $\gamma$. Since we only need the value of $C$ at irregular nodes $\mathcal{I}_h \subset \Omega_\gamma$, we only solve Cauchy problem for a short distance away from $\gamma$.

Let $\{\boldsymbol{q}_l\}_{l=1}^m \subset \gamma$ be a set of quasi-uniform distributed points on $\gamma$. Let $B_r(\boldsymbol{q}_l)$ be a ball centered at $\boldsymbol{q}_l$ with radius $r$. We set $r$ sufficiently large such that $\cup_{l=1}^M B_r(\boldsymbol{q}_l) \supset \Omega_\gamma$ and, typically, $r = \mathcal{O}(h)$. The numerical solution is represented using a partition of unity

$$C_h(\boldsymbol{x}) = \sum_{l=1}^{M} \omega_l(\boldsymbol{x}) C_{h,l}(\boldsymbol{x}), \qquad \boldsymbol{x} \in \cup_{l=1}^M B_r(\boldsymbol{q}_l). \tag{4.22}$$

where $\omega_l$ is an arbitrary partition of unity function subordinate to the ball $B_r(\boldsymbol{q}_l)$ and $C_{h,l}$ is the local solution in $B_r(\boldsymbol{q}_l)$. The simplest partition of unity is by defining it as

$$\omega_l(\boldsymbol{x}) = \begin{cases} 1, & l = \operatorname*{arginf}_k |\boldsymbol{q}_k - \boldsymbol{x}|, \\ 0, & \text{else}, \end{cases} \qquad \boldsymbol{x} \in \Omega_\gamma. \tag{4.23}$$

Such a partition of unity function is piecewise constant with value either 0 or 1, so that

$$C_h(\boldsymbol{x}) = C_{h,l}(\boldsymbol{x}), \qquad \text{if } l = \operatorname*{arginf}_k |\boldsymbol{q}_k - \boldsymbol{x}|. \tag{4.24}$$

In such way, we can separately solve the local solutions $C_{h,l}$ in each domain $B_r(\boldsymbol{q}_l)$. The local solution $C_{h,l}$ is represented as a linear combination of polynomial basis

$$C_{h,l}(\boldsymbol{x}) = \sum_{k=1}^{6} \alpha_{l,k}\phi_k\big(r^{-1}(\boldsymbol{x} - \boldsymbol{q}_l)\big), \qquad \boldsymbol{x} \in B_r(\boldsymbol{q}_l), \tag{4.25}$$

where $\alpha_{l,k}$ are the undetermined coefficients and $\phi_k$ is the monomial basis

$$\{\phi_j(x,y)\}_{j=1}^{6} = \{1, x, y, x^2, y^2, xy\}. \tag{4.26}$$

The prefactor $r^{-1}$ is designed to spatially rescale the local problem so the argument of $\phi_k$ has size $\mathcal{O}(1)$ rather than $\mathcal{O}(r)$.

We seek the value of $\alpha_{l,k}$ by collocation. We locally parameterize the curve segment $\gamma \cap B_r(\boldsymbol{q}_l)$ by $\boldsymbol{r}(s)$ for $s \in [-1, 1]$ with $\boldsymbol{r}(0) = \boldsymbol{q}_l$. Generally, one can select many collocation points from $B_r(\boldsymbol{q}_l)$ and $\gamma \cap B_r(\boldsymbol{q}_l)$ for the PDE and boundary conditions, to result in an overdetermined system and solve in the least squares sense. Here, to minimize computational cost, we will select the minimum number of collocation points to obtain a squared linear system based on [32]. We select collocation points $\{\boldsymbol{p}_{l,s}^{(1)}\}_{s=1}^{3}$ for the Dirichlet boundary condition, $\{\boldsymbol{p}_{l,s}^{(2)}\}_{s=1}^{2}$ for the Neumann boundary condition, and $\{\boldsymbol{p}_l^{(3)}\}$ for the PDE as

$$\begin{aligned} &\boldsymbol{p}_{l,1}^{(1)} = \boldsymbol{r}(0), \quad \boldsymbol{p}_{l,2}^{(1)} = \boldsymbol{r}(-1), \quad \boldsymbol{p}_{l,3}^{(1)} = \boldsymbol{r}(1), \\ &\boldsymbol{p}_{l,1}^{(2)} = \boldsymbol{r}(-1), \quad \boldsymbol{p}_{l,2}^{(2)} = \boldsymbol{r}(1), \quad \boldsymbol{p}_l^{(3)} = \boldsymbol{q}_l. \end{aligned} \tag{4.27}$$

Now we can form the discrete collocation problem as

$$\sum_{i,j=1}^{2} \partial_i \big(a_{ij}\partial_j C_{h,l}\big)(\boldsymbol{p}_l^{(3)}) - aC_{h,l}(\boldsymbol{p}_l^{(3)}) = \bar{f}(\boldsymbol{p}_l^{(3)}), \tag{4.28a}$$

$$rC_{h,l}(\boldsymbol{p}_{l,s}^{(1)}) = r\bar{\Phi}(\boldsymbol{p}_{l,s}^{(1)}), \qquad s = 1, 2, 3, \tag{4.28b}$$

$$r^2 \sum_{i,j=1}^{2} \beta_{ij}\partial_i C_{h,l}(\boldsymbol{p}_{l,s}^{(2)}) = r^2\bar{\Psi}(\boldsymbol{p}_{l,s}^{(2)}), \qquad s = 1, 2. \tag{4.28c}$$

In the above formulation, we have multiplied the both side of the Neumann boundary condition and the PDE by $r$ and $r^2$, respectively. This is equivalent to a diagonal preconditioning of the linear system, such that the resulting linear system has a much better condition number. The rescaling by $r^{-1}$ in the basis and the diagonal preconditioning combined render the resulting linear system insensitive to $r$. In practice, the linear system is always solvable with condition number $\sim \mathcal{O}(10^3)$ regardless of how small $r$ or $h$ is. Notice that forming the discrete linear system (4.28) requires derivatives of the coefficient $a_{ij}$. For ease of implementation, we adopt a hybrid finite difference-collocation approach where the derivatives in the PDE are replaced with finite differences.

## 5. Algorithm summary

Given a parametric representation of the interface curve, the parameter domain is sampled at $M$ quasi-uniformly spaced points with spacing approximately $1.5h$, and a cubic spline is fitted to these points for use in subsequent computations. Although the spline reconstruction is mathematically unnecessary when an exact parametric formula is available, this preprocessing step is included deliberately so that the algorithm handles interfaces specified only as discrete point clouds, as is common in practice.

Evaluated at these discrete points, the boundary integral Eqs. (3.12), (3.14), and (3.23)–corresponding to the respective Dirichlet, Neumann, and interface problems–are solved iteratively using the Generalized Minimal Residual (GMRES) method. At each iteration, all volume and boundary integrals are evaluated indirectly by solving the corresponding equivalent interface problems (4.1), utilizing the techniques developed in Sections 4.2 and 4.3. The modified discrete linear system (4.18) is inverted via a geometric multigrid method. The potential functions generated on the Cartesian grid are then accurately interpolated to the discrete interface points using Lagrange interpolation augmented with correction functions. Once the GMRES solver converges and the boundary integral equations are solved, the resulting densities are substituted into Eqs. (3.11), (3.13), or (3.21) to reconstruct the final numerical solution to the original surface PDEs.

The main algorithmic procedures are summarized in Algorithms 1 and 2.

**Algorithm 1:** Surface interface problem solver.

```
Initialization
1. Discretize the parameter domain $\Omega$ using a uniform Cartesian grid
2. Sample the interface $\Gamma$ with equal arc-length spacing, construct a cubic spline interpolant, and reparameterize
3. Classify grid nodes as either interior or exterior relative to the interface
Iterative Solution for the Boundary Integral Equations
1. Recast volume integrals, and single- and double-layer potentials as equivalent interface problems, then evaluate their
   values and normal derivatives on the interface via Algorithm 2
2. Initialize the respective density function, and iteratively solve the boundary integral equations via GMRES until reaching
   the specified error tolerance
Reconstruction of the Original PDE Solution
1. Compute the volume integrals, and the single- and double-layer potentials at the Cartesian grid nodes using the first three
   steps of Algorithm 2
2. Superpose the computed potential functions according to the representation formula to obtain the final numerical solution
```

```
Algorithm 2: Boundary data computation.
1. Discretize the equivalent interface problem using the standard 7-point finite difference scheme
2. Solve the local Cauchy problems via the collocation method to obtain the correction function and correct the right-hand
   side of the linear system
3. Invert the modified linear system using a geometric multigrid solver to obtain the potential functions on the Cartesian grid
4. Extract the necessary function values and normal derivatives at the interface points via correction-augmented Lagrange
   interpolation
```

We conclude this section with a brief analysis of the computational complexity. Assume the planar domain is partitioned into an $N \times N$ Cartesian grid. Since the interface point spacing scales with $h$, the number of interface points $M$ is $\mathcal{O}(N)$. In each GMRES iteration, the equivalent interface problems are solved via the geometric multigrid method at a cost of $\mathcal{O}(N^2)$ operations, while solving the $M$ local $6 \times 6$ Cauchy systems and performing Lagrange interpolation contributes only $\mathcal{O}(N)$ work. Thus, if the GMRES iteration count is independent of $N$, the total computational complexity of the method is $\mathcal{O}(N^2)$.

## 6. Numerical experiments

In this section, we present numerical results for several elliptic partial differential equations on complex bounded regions of surfaces. These equations encompass boundary value problems that include both Dirichlet and Neumann conditions, as well as interface problems on bounded regions of surfaces and interface problems on singly periodic irregular domains.

Throughout these experiments, the following two types of closed curves are primarily considered as the preimage of the interface $\Gamma \subset \mathcal{S}$:

- Case I: A rotated ellipse

$$\begin{cases} x = r_a \cos\theta\cos\alpha - r_b \sin\theta\sin\alpha, \\ y = r_a \cos\theta\sin\alpha + r_b \sin\theta\cos\alpha, \end{cases} \qquad \text{for } \theta \in [0, 2\pi), \tag{6.1}$$

  where $\alpha$ is the rotation angle, $r_a$ and $r_b$ are the major and minor radii of the ellipse, respectively.

- Case II: A star-shaped domain

$$\begin{cases} x = \left[r_a + \epsilon\cos(m\theta)\right]\cos(\theta+\alpha), \\ y = \left[r_b + \epsilon\cos(m\theta)\right]\sin(\theta+\alpha), \end{cases} \qquad \text{for } \theta \in [0, 2\pi), \tag{6.2}$$

  where $m$ represents the fold number and $\epsilon$ is a constant.

In each test, the GMRES solver starts with a zero initial guess, and the convergence tolerance is fixed at $\texttt{tol} = 1.0 \times 10^{-8}$. The numerical results are summarized through tables and figures. Each table reports the following metrics: the Cartesian grid size, the total number of discretization points on the boundary curve, the required number of GMRES iterations, the maximum discrete error of the numerical solution at the interior grid nodes, and the CPU time in seconds. The numerical algorithm is implemented in C++, and all computations are performed on a personal computer equipped with an Intel Core i9-11900H CPU @ 2.50GHz and 16 GB of RAM.

**Example 6.1.** In this example, the boundary value problems (2.8) subject to both the Dirichlet boundary conditions (2.9) and the Neumann boundary conditions (2.10) are addressed. The underlying surface $\mathcal{S}$ is parametrized by

$$\begin{aligned} \boldsymbol{X} :\ & [-1,1]^2 \to \mathbb{R}^3, \\ & (u, v) \mapsto (3u + v, u - 2v, u^3 + v^3). \end{aligned} \tag{6.3}$$

The preimage of the interface $\Gamma$ is taken to be a rotated ellipse in Case I, with the parameters given as follows:

$$r_a = 0.7, \qquad r_b = 0.4, \qquad \alpha = 3\pi/5. \tag{6.4}$$

And the Dirichlet and Neumann boundary conditions on $\Gamma$ are prescribed such that the exact solution reads

$$u(x, y, z) = \mathrm{e}^{\frac{2x+y}{7}} \cos\frac{x - 3y}{7}, \qquad (x, y, z) \in \mathcal{S}, \tag{6.5}$$

with $\kappa = 5$.

Numerical results are summarized in Table 1 for the Dirichlet condition and Table 2 for the Neumann condition. Corresponding visualizations are illustrated in Figs. 2 and 3, respectively. For the Dirichlet boundary condition (Table 1), the observed convergence order is slightly above second order, approaching third order on some grids. This is because the trace of the solution on the interface is recovered via quadratic interpolation, which is third-order accurate for function values. For the Neumann condition, the interpolation targets the normal derivative, which reduces the accuracy to second order. Since the interpolation order exceeds that of the finite difference scheme on coarser grids, super-second-order convergence is observed; the rate is expected to approach two asymptotically as $h \to 0$.

**Table 1**
Numerical results for the Dirichlet boundary condition in Example 6.1.

| Grid size | $64 \times 64$ | $128 \times 128$ | $256 \times 256$ | $512 \times 512$ | $1024 \times 1024$ |
|---|---|---|---|---|---|
| M | 75 | 150 | 300 | 601 | 1202 |
| #GMRES | 7 | 6 | 5 | 5 | 5 |
| CPU (s) | 8.40E-1 | 3.01E+0 | 1.07E+1 | 4.47E+1 | 1.85E+2 |
| $\|\mathbf{e}_h\|_\infty$ | 5.56E-4 | 8.97E-5 | 2.08E-5 | 2.11E-6 | 2.84E-7 |
| Order | - | 2.63 | 2.11 | 3.30 | 2.89 |

**Table 2**
Numerical results for the Neumann boundary condition in Example 6.1.

| Grid size | $64 \times 64$ | $128 \times 128$ | $256 \times 256$ | $512 \times 512$ | $1024 \times 1024$ |
|---|---|---|---|---|---|
| M | 75 | 150 | 300 | 601 | 1202 |
| #GMRES | 7 | 6 | 6 | 6 | 6 |
| CPU (s) | 9.16E-1 | 2.89E+0 | 1.21E+1 | 4.85E+1 | 1.92E+2 |
| $\|\mathbf{e}_h\|_\infty$ | 1.44E-1 | 3.37E-2 | 1.02E-2 | 2.43E-3 | 6.23E-4 |
| Order | - | 2.10 | 1.72 | 2.07 | 1.96 |

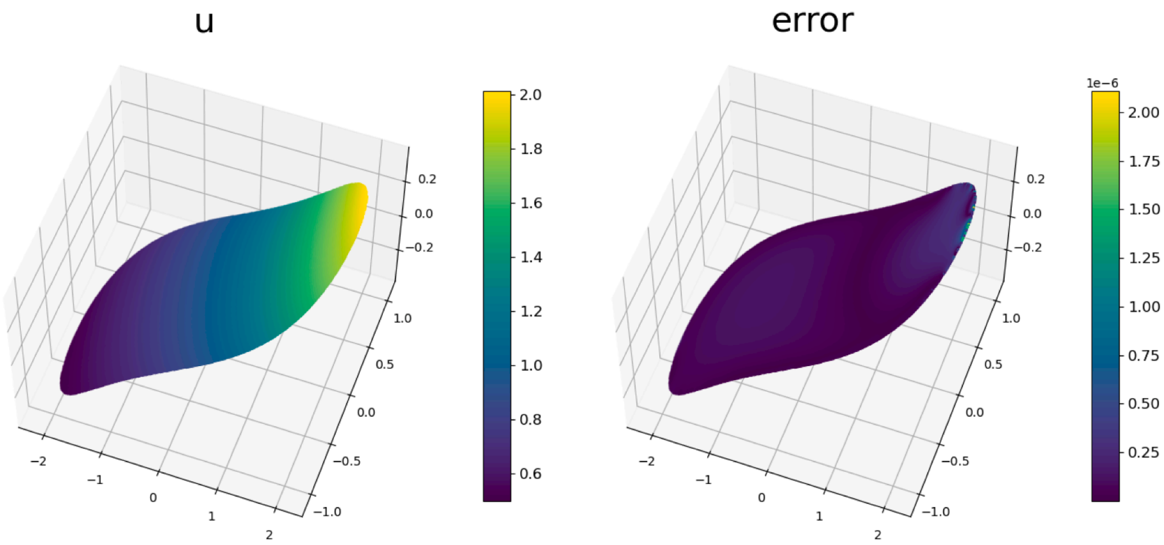

**Fig. 2.** The numerical solution and the pointwise absolute error in Example 6.1 for the Dirichlet boundary condition on the $512 \times 512$ grid.

**Example 6.2** (A helicoid surface). This example considers the interface problem (2.12) on a helicoid surface $\mathcal{S}$ given by

$$\begin{aligned} \boldsymbol{X} :\ & [-1,1]^2 \to \mathbb{R}^3, \\ & (u,v) \mapsto (u \sin v, u \cos v, v), \end{aligned} \tag{6.6}$$

where $\frac{\kappa^+}{\beta^+} = \frac{\kappa^-}{\beta^-} = 1$, with $\beta^+ = \kappa^+ = 3$ and $\beta^- = \kappa^- = 1$. A circle with radius of 0.5 is used as the preimage of the interface $\Gamma \subset \mathcal{S}$. The interior and exterior exact solutions of the equation read

$$\begin{aligned} u^+(x,y,z) &= \sin x \sin y \sin z, \\ u^-(x,y,z) &= (x^2 - z - 1)(y^2 + z - 1), \end{aligned} \qquad (x,y,z) \in \mathcal{S}. \tag{6.7}$$

Corresponding numerical results for Example 6.2 are displayed in Table 3 and Fig. 4.

The results indicate that the proposed KFBI method achieves second-order convergence for elliptic interface problems. The low iteration counts and CPU times demonstrate the high computational efficiency of the proposed method.

**Example 6.3** (A saddle surface). This example solves the interface problem (2.12) on a saddle surface defined by

$$\begin{aligned} \boldsymbol{X} :\ & [-1,1]^2 \to \mathbb{R}^3, \\ & (u,v) \mapsto \left(u, v, u^2 - v^2\right). \end{aligned} \tag{6.8}$$

The interface $\Gamma$ is determined by a star-shaped domain in Case II with the parameters chosen as:

$$r_a = 0.7, \qquad r_b = 0.4, \qquad \alpha = 6\pi/7, \qquad \epsilon = 0.3, \qquad m = 3. \tag{6.9}$$

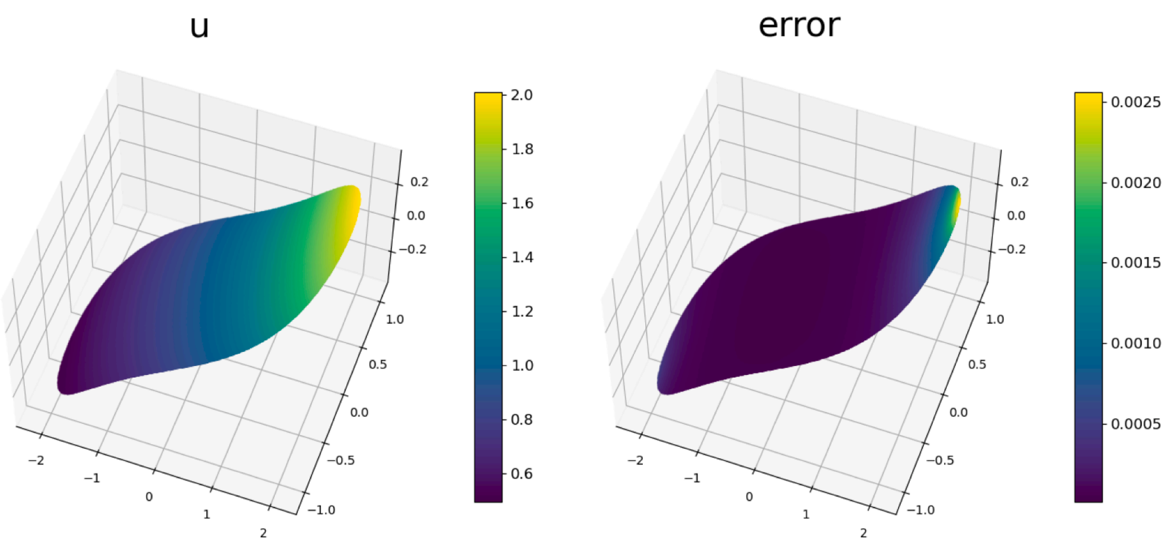

**Fig. 3.** The numerical solution and the pointwise absolute error in Example 6.1 for the Neumann boundary condition on the $512 \times 512$ grid.

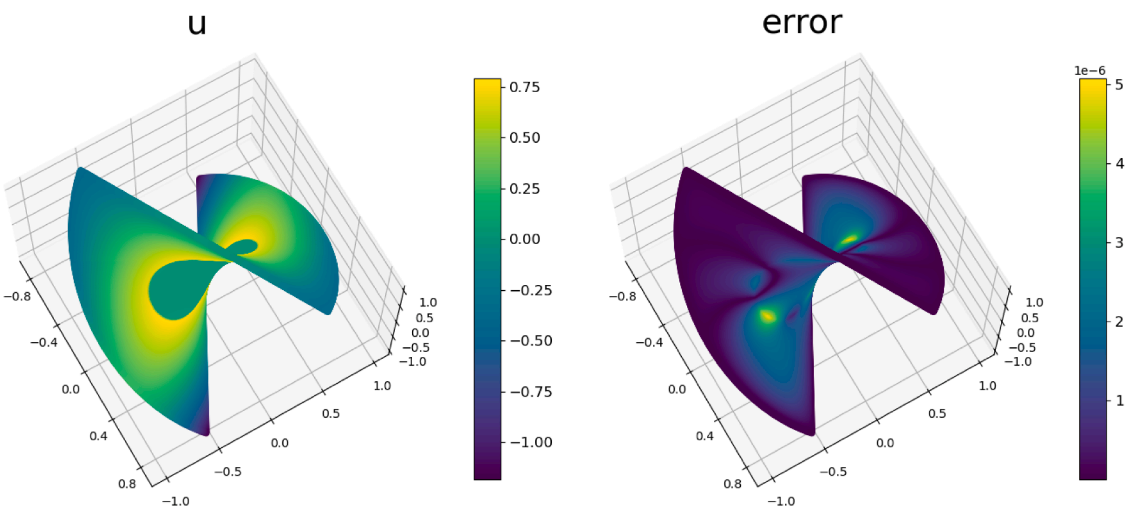

**Fig. 4.** The numerical solution and the pointwise absolute error in Example 6.2 on the $512 \times 512$ grid.

**Table 3**
Numerical results for the interface problem in Example 6.2.

| Grid size | $64 \times 64$ | $128 \times 128$ | $256 \times 256$ | $512 \times 512$ | $1024 \times 1024$ |
|---|---|---|---|---|---|
| M | 67 | 134 | 268 | 536 | 1072 |
| #GMRES | 7 | 6 | 6 | 6 | 6 |
| CPU (s) | 9.64E-1 | 3.15E+0 | 1.26E+1 | 4.93E+1 | 1.97E+2 |
| $\|\mathbf{e}_h\|_\infty$ | 3.48E-4 | 8.70E-5 | 2.36E-5 | 5.08E-6 | 1.23E-6 |
| Order | - | 2.00 | 1.88 | 2.22 | 2.04 |

The exact solutions to the equation in the interior and exterior regions are

$$\begin{aligned} u^+(x, y, z) &= ze^x \cos y, \\ u^-(x, y, z) &= ze^y \sin x, \end{aligned} \qquad (x, y, z) \in \mathcal{S}. \tag{6.10}$$

For this example, the grid size is fixed at $128 \times 128$. The ratio $\kappa/\beta$ for both the interior and exterior regions is set to a constant $c$, i.e., $\frac{\kappa^+}{\beta^+} = \frac{\kappa^-}{\beta^-} = c$. By substantially varying the magnitude of $c$, we demonstrate that the proposed method remains robust even under exceptionally high and low contrast regimes. The results are presented in Table 4.

**Table 4**

Numerical results for the interface problem in Example 6.3 on the $128 \times 128$ grid for $c = 1.0 \times 10^{\pm 3}$.

| $\kappa^+$ | 1.2E+3 | 1.2E-3 | 2.0E+0 | 2.0E+0 |
|---|---|---|---|---|
| $\kappa^-$ | 8.0E+2 | 8.0E-4 | 7.0E-1 | 7.0E-1 |
| $\beta^+$ | 1.2E+0 | 1.2E+0 | 2.0E-3 | 2.0E+3 |
| $\beta^-$ | 8.0E-1 | 8.0E-1 | 7.0E-4 | 7.0E+2 |
| $c$ | 1.0E+3 | 1.0E-3 | 1.0E+3 | 1.0E-3 |
| #GMRES | 7 | 8 | 9 | 13 |
| $\Vert\mathbf{e}_h\Vert_\infty$ | 7.15E-5 | 7.40E-4 | 7.22E-5 | 9.97E-4 |

**Table 5**

Numerical results for the interface problem in Example 6.3 with different coefficient ratios $q = \beta^+/\beta^-$.

| Grid size | $\beta^+ = 1$, $\beta^- = 1000$, $q = 0.001$ | | | $\beta^+ = 1$, $\beta^- = 2$, $q = 0.5$ | | | $\beta^+ = 1$, $\beta^- = 0.001$, $q = 1000$ | | |
|---|---|---|---|---|---|---|---|---|---|
| | #GMRES | $\Vert\mathbf{e}_h\Vert_\infty$ | Order | #GMRES | $\Vert\mathbf{e}_h\Vert_\infty$ | Order | #GMRES | $\Vert\mathbf{e}_h\Vert_\infty$ | Order |
| $64 \times 64$ | 16 | 1.78E-3 | - | 10 | 1.89E-3 | - | 18 | 9.44E-3 | - |
| $128 \times 128$ | 16 | 5.21E-4 | 1.77 | 10 | 5.18E-4 | 1.87 | 20 | 2.63E-3 | 1.85 |
| $256 \times 256$ | 16 | 1.16E-4 | 2.16 | 10 | 1.18E-4 | 2.13 | 20 | 6.33E-4 | 2.05 |
| $512 \times 512$ | 16 | 2.97E-5 | 1.97 | 10 | 3.03E-5 | 1.97 | 20 | 1.71E-4 | 1.87 |
| $1024 \times 1024$ | 16 | 7.44E-6 | 2.00 | 10 | 7.59E-6 | 2.00 | 19 | 4.49E-6 | 1.93 |

**Table 6**

Numerical results for the interface problem in Example 6.4.

| Grid size | $64 \times 64$ | $128 \times 128$ | $256 \times 256$ | $512 \times 512$ | $1024 \times 1024$ |
|---|---|---|---|---|---|
| M | 118 | 237 | 473 | 946 | 1892 |
| #GMRES | 10 | 10 | 9 | 10 | 10 |
| CPU (s) | 7.09E+0 | 2.77E+1 | 1.00E+2 | 4.37E+2 | 1.99E+3 |
| $\Vert\mathbf{e}_h\Vert_\infty$ | 4.10E-3 | 8.66E-4 | 1.96E-4 | 5.63E-5 | 1.38E-5 |
| Order | - | 2.24 | 2.15 | 1.80 | 2.03 |

Next, while maintaining $c = 1$, we define $q = \beta^+/\beta^-$ as the interior-to-exterior ratio of the parameter $\beta$. We investigate the algorithm's robustness across different coefficient magnitudes by systematically varying $q$; detailed results are provided in Table 5.

**Example 6.4** (An elliptic paraboloid surface). This example considers the interface problem (2.12) on an elliptic paraboloid surface $\mathcal{S}$ given by

$$\begin{aligned} \boldsymbol{X} :\ & [-1.4, 1.4]^2 \to \mathbb{R}^3, \\ & (u, v) \mapsto \left(u, v, u^2 + v^2\right), \end{aligned} \tag{6.11}$$

where $\frac{\kappa^+}{\beta^+} = 3$, $\frac{\kappa^-}{\beta^-} = 0.5$. The interface $\Gamma$ is determined by a star-shaped domain in Case II with the parameters chosen as:

$$r_a = 0.7, \qquad r_b = 0.7, \qquad \alpha = 11\pi/13, \qquad \epsilon = 0.3, \qquad m = 5. \tag{6.12}$$

The interior and exterior exact solutions of the equation read

$$\begin{aligned} u^+(x, y, z) &= \cos(x + y)\sin z, \\ u^-(x, y, z) &= (x^2 - 1)(y^2 - 1), \end{aligned} \qquad (x, y, z) \in \mathcal{S}. \tag{6.13}$$

Corresponding numerical results are displayed in Table 6 and Fig. 5. Example 6.4 considers the case where the ratio $\kappa/\beta$ differs across the interface. The numerical results indicate that, analogous to the uniform ratio case, the KFBI method consistently maintains second-order convergence alongside high computational efficiency.

We now fix $\kappa^\pm = 1$ and $\beta^+ = 1$, while varying $\beta^-$ to examine the influence of differing interior-exterior conductivity ratios on computational performance. As previously demonstrated, the required number of GMRES iterations is independent of grid refinement; consequently, iteration counts are omitted here. The corresponding maximum norm errors and CPU times are depicted in Figs. 6 and 7.

**Example 6.5** (A torus). In this example, we consider the interface problem on a torus $\mathbb{T}^2 \subset \mathbb{R}^3$ with a global parametrization given by

$$\begin{aligned} \boldsymbol{X} :\ & (\mathbb{R}/2\pi\mathbb{Z})^2 \to \mathbb{R}^3 \\ & (u, v) \mapsto ((R + r\sin u)\cos v, (R + r\sin u)\sin v, r\cos u), \end{aligned} \tag{6.14}$$

where $R, r > 0$ are the major and minor radii, respectively. Parameters are taken as follows:

$$R = 2.0, \qquad r = 0.8, \tag{6.15a}$$

$$\beta^\pm = 1.25 \pm 0.75, \qquad \kappa^\pm = 1.25 \pm 0.75. \tag{6.15b}$$

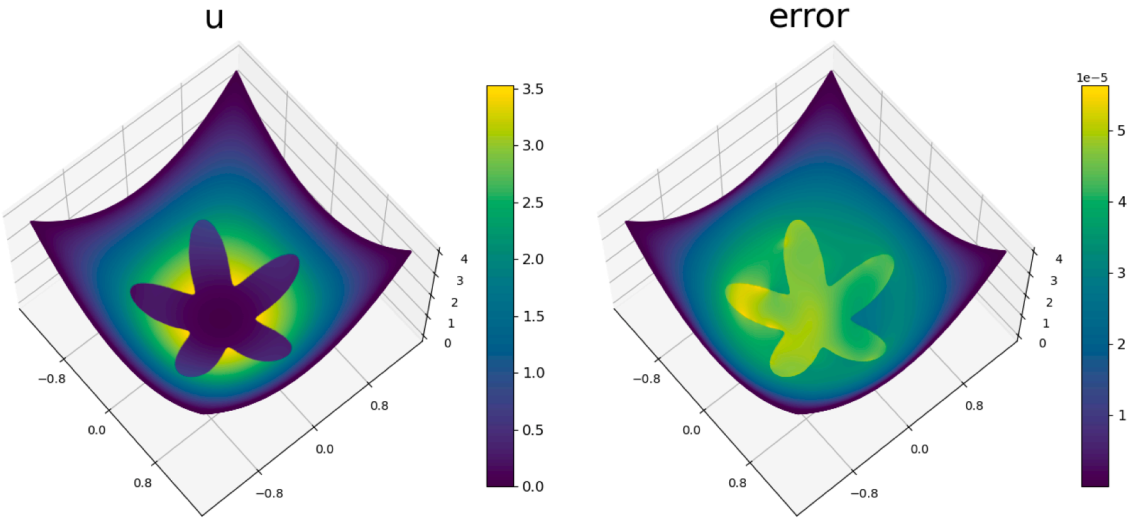

**Fig. 5.** The numerical solution and the pointwise absolute error in Example 6.4 on the 512 × 512 grid.

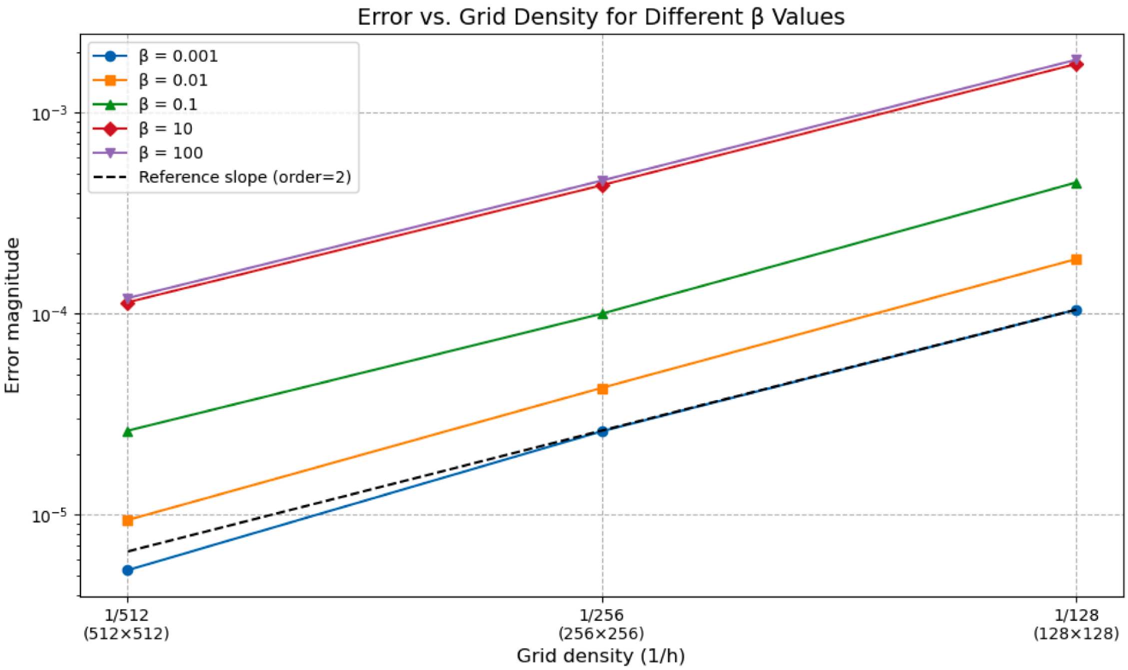

**Fig. 6.** The maximum norm error in Example 6.4 with different interior-to-exterior $\beta$ ratios.

Two types of surfaces $\Gamma_1$ and $\Gamma_2$ in Case I and Case II are selected as test-case interfaces, with their respective parameter chosen as:

$$\begin{aligned} &\Gamma_1: \quad r_a = 1.0, \quad r_b = 0.6, \quad \alpha = 9\pi/13, \\ &\Gamma_2: \quad r_a = 0.6, \quad r_b = 0.6, \quad \alpha = \pi/4, \quad \epsilon = 0.4, \quad m = 3. \end{aligned} \tag{6.16}$$

The interior and exterior exact solutions of the equation read

$$\begin{aligned} u^+(u,v) &= \sin u \cos v, \\ u^-(u,v) &= \cos u \sin v, \end{aligned} \qquad (u,v) \in \Omega. \tag{6.17}$$

The numerical solutions and pointwise absolute errors for $\Gamma_1$ and $\Gamma_2$ are shown in Figs. 8 and 9, respectively. The convergence study for $\Gamma_1$ is reported in Table 7, which lists the GMRES iteration counts, CPU times, and maximum errors under successive grid refinement. The results confirm second-order convergence.

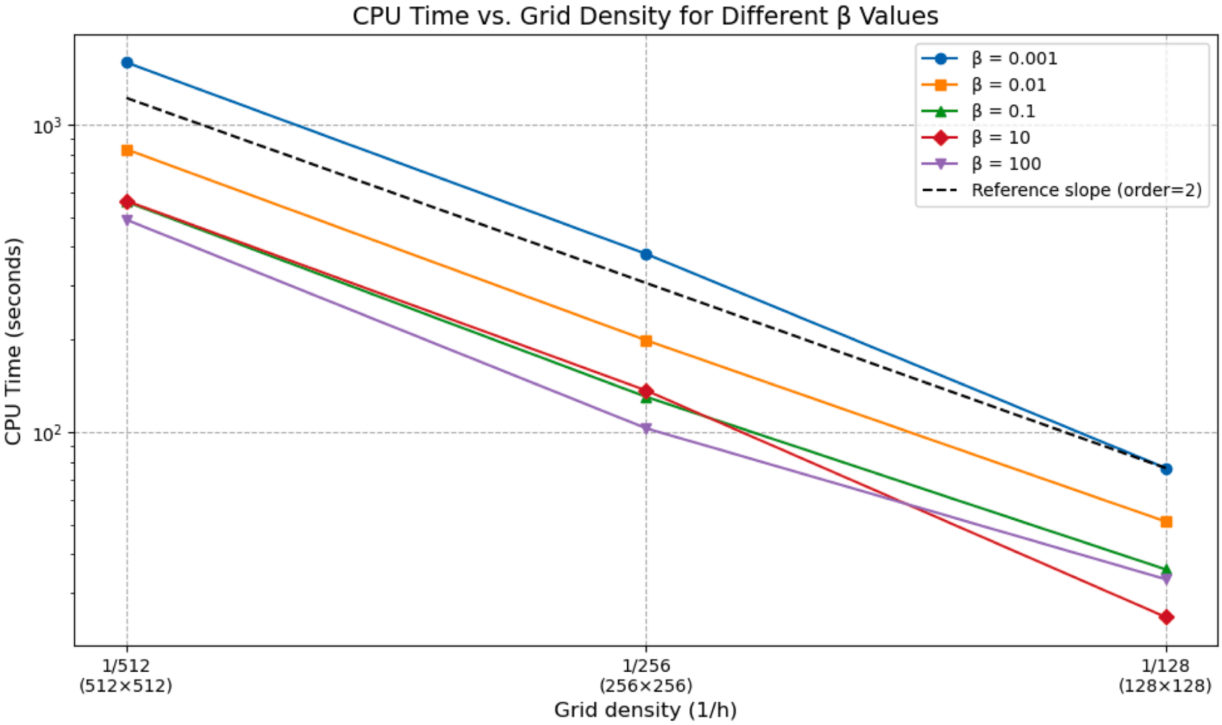

**Fig. 7.** The CPU time in Example 6.4 with different interior-to-exterior $\beta$ ratios.

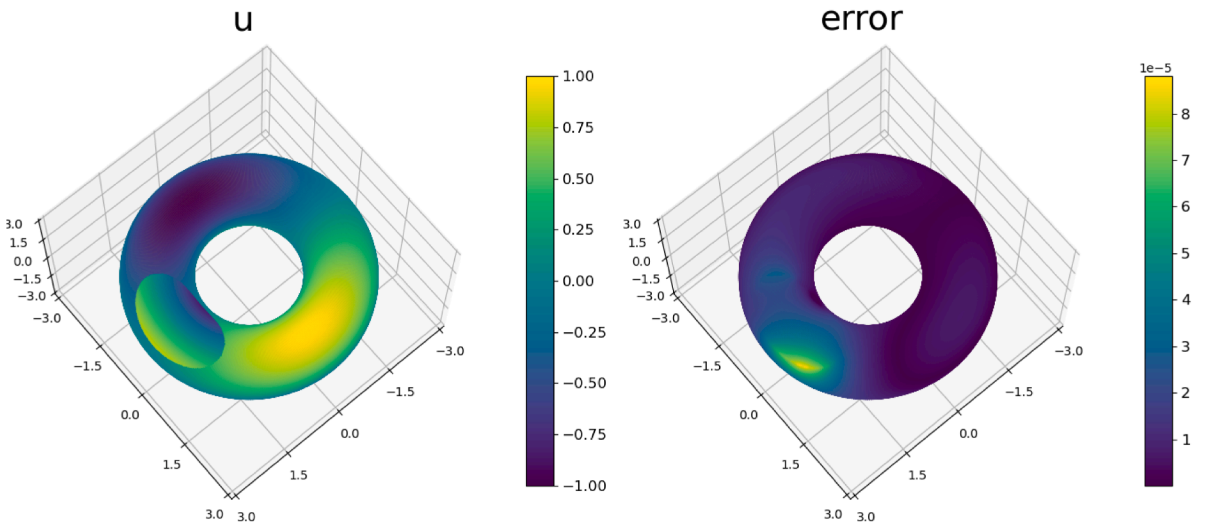

**Fig. 8.** The numerical solution and the pointwise absolute error in Example 6.5 of $\Gamma_1$ on the $512 \times 512$ grid.

**Example 6.6** (A torus)**.** In this example, the parametric surface, the coefficients $\beta$, and the exact solutions are the same as in Example 6.5, with $\Gamma$ taken as a unit circle. Here we consider the special case where $\kappa = 0$.

This example is treated separately because the interface problem on a closed surface with $\kappa = 0$ admits a nontrivial null space, making the solution unique only up to an additive constant. Without special treatment, the multigrid solver fails to converge. To address this, a mean-zero constraint is enforced at the coarsest grid level by subtracting the mean from the solution before each coarse-grid correction [52]. After convergence, the final solution is further shifted to have zero mean. The reported errors are computed modulo this additive constant.

The numerical results are presented in Table 8, and the numerical solution with pointwise absolute error is shown in Fig. 10.

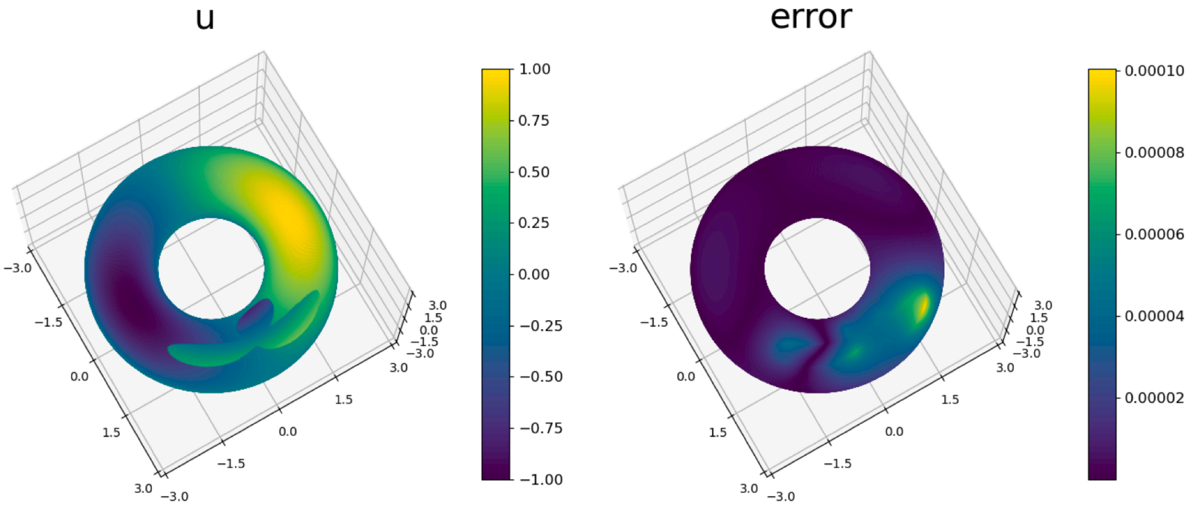

**Fig. 9.** The numerical solution and the pointwise absolute error in Example 6.5 of $\Gamma_2$ on the 512 × 512 grid.

**Table 7**
Numerical results for the interface problem in Example 6.5 of $\Gamma_1$.

| Grid size | 64 × 64 | 128 × 128 | 256 × 256 | 512 × 512 | 1024 × 1024 |
|---|---|---|---|---|---|
| M | 44 | 87 | 175 | 350 | 700 |
| #GMRES | 17 | 17 | 17 | 14 | 15 |
| CPU (s) | 3.70E+0 | 1.53E+1 | 6.20E+1 | 2.13E+2 | 1.06E+3 |
| $\|\mathbf{e}_h\|_\infty$ | 1.37E-2 | 2.12E-3 | 3.56E-4 | 1.00E-4 | 2.09E-5 |
| Order | - | 2.69 | 2.58 | 1.83 | 2.26 |

**Table 8**
Numerical results for the interface problem in Example 6.6.

| Grid size | 64 × 64 | 128 × 128 | 256 × 256 | 512 × 512 | 1024 × 1024 |
|---|---|---|---|---|---|
| M | 43 | 85 | 171 | 341 | 683 |
| #GMRES | 10 | 10 | 10 | 10 | 10 |
| CPU (s) | 2.75E+0 | 1.13E+1 | 4.61E+1 | 1.82E+2 | 7.52E+2 |
| $\|\mathbf{e}_h\|_\infty$ | 1.36E-2 | 2.74E-3 | 7.89E-4 | 2.26E-4 | 5.90E-5 |
| Order | - | 2.31 | 1.80 | 1.80 | 1.94 |

**Example 6.7** (An elliptical torus). In this example, we employ an elliptical torus $\mathbb{T}^2 \subset \mathbb{R}^3$ as the computational surface, whose global parametric representation is given as follows:

$$\begin{aligned} \boldsymbol{X} : \; & (\mathbb{R}/2\pi\mathbb{Z})^2 \to \mathbb{R}^3 \\ & (u, v) \mapsto ((R + a\sin u)\cos v, (R + a\sin u)\sin v, b\cos u), \end{aligned} \tag{6.18}$$

where $R$ denotes the radius of revolution, and $a$, $b$ are the semi-major and semi-minor axes of the elliptical cross-section, respectively. The interface $\Gamma$ is determined by a star-shaped domain in Case II with the parameters chosen as:

$$r_a = 0.7, \qquad r_b = 0.7, \qquad \alpha = 0, \qquad \epsilon = 0.5, \qquad m = 5. \tag{6.19}$$

Unlike the previous examples, no exact solution is prescribed *a priori*. Instead, the interface conditions are determined solely by the intrinsic geometric properties of the surface. Specifically, the interface problem reads:

$$\nabla_{\mathcal{S}} \cdot \left(\beta \nabla_{\mathcal{S}} u\right) - \kappa u = 0, \qquad \text{in } \mathcal{S} \setminus \Gamma, \tag{6.20}$$

subject to the following conditions:

$$\begin{aligned} [u] &= H, && \text{on } \Gamma, \\ [\beta \nu \cdot \nabla_{\mathcal{S}} u] &= K, && \text{on } \Gamma, \end{aligned} \tag{6.21}$$

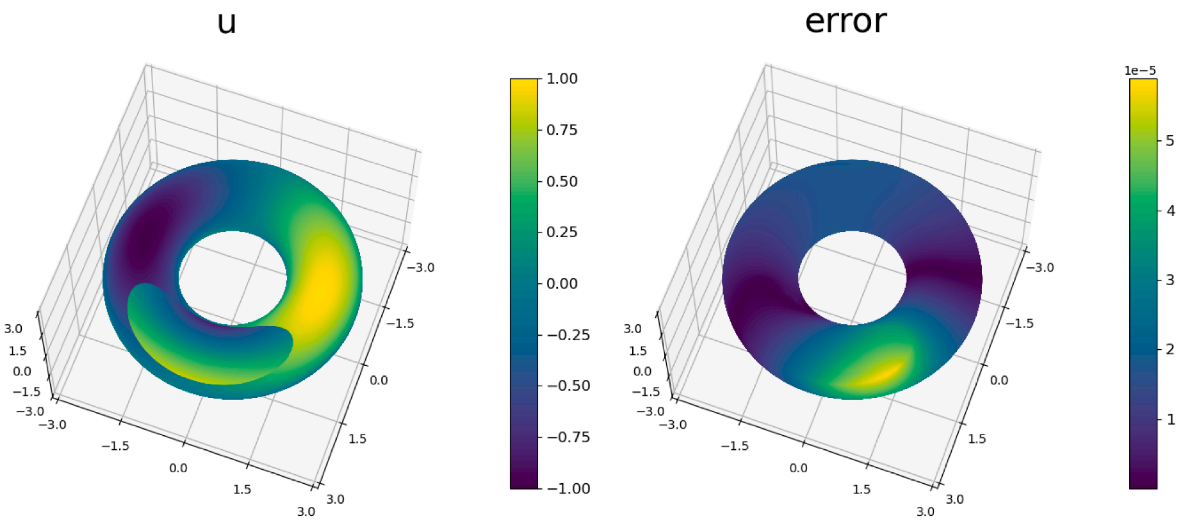

**Fig. 10.** The numerical solution and the pointwise absolute error in Example 6.6 on the 1024 × 1024 grid.

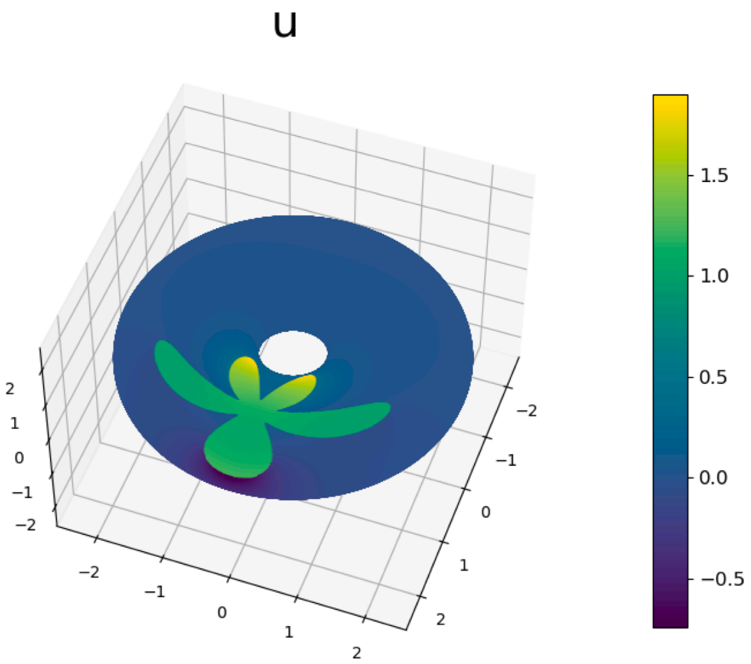

**Fig. 11.** The numerical solution in Example 6.7 on the 1024 × 1024 grid.

where $H$ and $K$ denote the mean and Gaussian curvatures of the surface, respectively, given by the standard differential geometry formulas:

$$\begin{aligned} H &= \frac{1}{2}\left(\frac{a}{b(R+a\sin u)} + \frac{b(R+a\sin u)}{a^2\cos^2 u + b^2\sin^2 u}\right), \\ K &= \frac{ab}{(a^2\cos^2 u + b^2\sin^2 u)(R+a\sin u)^2}, \end{aligned} \tag{6.22}$$

The parameters are $R = 1.5$, $a = 1.0$, $b = 0.6$, $\beta^+ = 2.0$, $\beta^- = 0.5$, $\kappa^+ = 2.0$, and $\kappa^- = 0.5$. The numerical solution on a $1024 \times 1024$ grid is depicted in Fig. 11. The computation required 17 GMRES iterations and a total CPU time of 1139.77 s. This example confirms that the proposed method remains efficient and accurate when the interface conditions are determined by the intrinsic geometry of the surface.

**Table 9**
Numerical results for the interface problem in Example 6.8.

| Grid size | $64 \times 64$ | $128 \times 128$ | $256 \times 256$ | $512 \times 512$ | $1024 \times 1024$ |
|---|---|---|---|---|---|
| M | 43 | 85 | 171 | 341 | 683 |
| #GMRES | 8 | 8 | 8 | 7 | 7 |
| CPU (s) | 6.43E+0 | 2.55E+1 | 9.97E+1 | 3.22E+2 | 1.39E+3 |
| $\|\mathbf{e}_h\|_\infty$ | 7.44E-3 | 1.95E-3 | 5.03E-4 | 1.22E-4 | 3.10E-5 |
| Order | - | 1.93 | 1.96 | 2.04 | 1.97 |

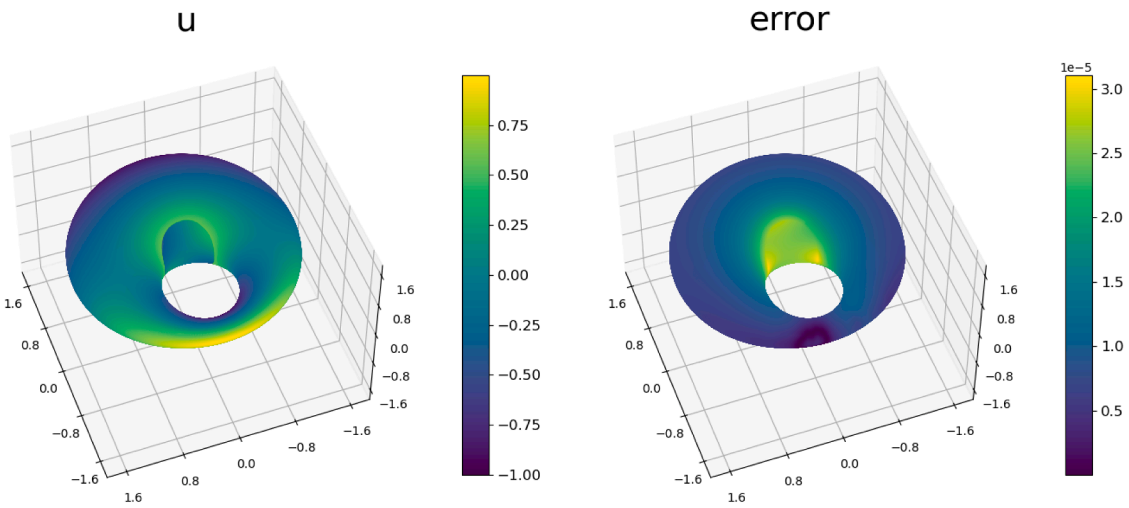

**Fig. 12.** The numerical solution and the pointwise absolute error in Example 6.8 on the $1024 \times 1024$ grid.

**Example 6.8** (A Dupin cyclide). This example considers the interface problem on a Dupin cyclide $\mathcal{D} \subset \mathbb{R}^3$, whose parametrization is given by

$$\begin{aligned} &\boldsymbol{X} : (\mathbb{R}/2\pi\mathbb{Z})^2 \to \mathbb{R}^3 \\ &(u, v) \mapsto \left( \frac{d(c - a\cos u \cos v) + b^2 \cos u}{a - c\cos u \cos v}, \frac{b \sin u\,(a - d\cos v)}{a - c\cos u \cos v}, \frac{b \sin v\,(c\cos u - d)}{a - c\cos u \cos v} \right). \end{aligned} \tag{6.23}$$

The parameters are chosen as $a = 1, b = 1, c = -0.3, d = 0.5$. The diffusion and reaction coefficients are $\beta^\pm = 1.9 \pm 1.1$ and $\kappa^\pm = 1.9 \pm 1.1$. The preimage of the interface in parameter space is a unit circle, and the interior and exterior exact solutions are

$$\begin{aligned} u^+(u, v) &= \sin u \sin v, \\ u^-(u, v) &= \cos u \cos v, \end{aligned} \qquad (u, v) \in \Omega. \tag{6.24}$$

The numerical results are summarized in Table 9 and the solution profile is depicted in Fig. 12.

## 7. Conclusion

This study develops an efficient kernel-free boundary integral method for accurately solving elliptic boundary value and interface problems on surfaces. The proposed method reformulates the original problem as boundary integral equations, and evaluates the resulting singular integrals indirectly by solving equivalent interface problems on Cartesian grids via a geometric multigrid method. This strategy avoids the difficulties associated with mesh transformation and direct numerical quadrature. The combination of boundary integral equations with finite difference methods enables the proposed approach to effectively handle complex geometric interfaces and discontinuities near the interface, offering broad applicability.

The proposed method offers several key advantages, including flexible treatment of complex geometries, high computational efficiency, robust convergence rates, and mesh-independent convergence behavior of the iterative solvers. Numerical results demonstrate that the method maintains second-order accuracy regardless of whether the interior/exterior $\kappa$ and $\beta$ ratios are equal or unequal, while showing robust applicability across wide $\beta$ variations. For interface problems on closed surfaces with periodic boundary conditions, the proposed method maintains second-order convergence and exhibits favorable computational efficiency.

The current method is confined to surfaces that possess a regular global parameterization. Nevertheless, such a parameterization is not available for general closed surfaces. Despite this limitation, the current potential theory-based approach offers a framework for efficiently solving interface problems on surfaces through an immersed interface-type technique. To extend the applicability of this method to a wider range of closed surfaces, we will employ alternative surface and interface discretization techniques and numerical schemes, such as those described in [53] and [19].

## CRediT authorship contribution statement

**Pengsong Yin:** Writing – original draft, Visualization, Software, Methodology, Investigation, Conceptualization; **Wenjun Ying:** Writing – review & editing, Supervision, Funding acquisition; **Yulin Zhang:** Writing – review & editing, Supervision, Project administration, Conceptualization; **Han Zhou:** Writing – review & editing, Supervision, Project administration, Methodology.

## Data availability

Data will be made available on request.

## Declaration of competing interest

The authors declare that they have no known competing financial interests or personal relationships that could have appeared to influence the work reported in this paper.

## Acknowledgement

The authors thank the anonymous reviewers for their valuable and constructive suggestions. W. Ying is supported by the National Natural Science Foundation of China in the Division of Mathematical Sciences (Project No. 12471342).

## References

[1] J. Isern-Fontanet, J. Ballabrera-Poy, A. Turiel, E. García-Ladona, Remote sensing of ocean surface currents: a review of what is being observed and what is being assimilated, Nonlin. Process. Geophys. 24 (2017) 613–643.
[2] D. Langevin, Rheology of adsorbed surfactant monolayers at fluid surfaces, Annu. Rev. Fluid Mech. 46 (2014) 47–65.
[3] M. Muradoglu, G. Tryggvason, Simulations of soluble surfactants in 3D multiphase flow, J. Comput. Phys. 274 (2014) 737–757.
[4] B. Cushman-Roisin, J. Beckers, Introduction to geophysical fluid dynamics: physical and numerical aspects, Academic press, 2011.
[5] W. Lowrie, A. Fichtner, Fundamentals of geophysics, Cambridge University Press, 2020.
[6] M. Olshanskii, A. Quaini, A. Reusken, V. Yushutin, A finite element method for the surface stokes problem, SIAM J. Sci. Comput. 40 (2018) A2492–A2518.
[7] S. Reuther, A. Voigt, Solving the incompressible surface navier-Stokes equation by surface finite elements, Phys. Fluids 30 (1) (2018).
[8] P. Gera, D. Salac, Modeling of multicomponent three-dimensional vesicles, Comput. Fluids 172 (2018) 362–383.
[9] C. Elliott, B. Stinner, Modeling and computation of two phase geometric biomembranes using surface finite elements, J. Comput. Phys. 229 (2010) 6585–6612.
[10] K. Cheng, C. Wang, S.M. Wise, A weakly nonlinear, energy stable scheme for the strongly anisotropic Cahn-Hilliard equation and its convergence analysis, J. Comput. Phys. 405 (2020) 109109.
[11] K. Cheng, C. Wang, S.M. Wise, High order accurate and convergent numerical scheme for the strongly anisotropic Cahn–Hilliard model, Numer. Methods Partial Differ. Equ. 39 (5) (2023) 4007–4029.
[12] G. Dziuk, C. Elliott, Surface finite elements for parabolic equations, J. Comput. Math. 25 (2007) 385–407.
[13] G. Dziuk, C. Elliott, Finite element methods for surface PDEs, Acta Numer. 22 (2013) 289–396.
[14] A. Demlow, M. Olshanskii, An adaptive surface finite element method based on volume meshes, SIAM J. Numer. Anal. 50 (2012) 1624–1647.
[15] L. Ju, Q. Du, A finite volume method on general surfaces and its error estimates, J. Math. Anal. Appl. 352 (2009) 645–668.
[16] D. Calhoun, C. Helzel, A finite volume method for solving parabolic equations on logically cartesian curved surface meshes, SIAM J. Sci. Comput. 31 (2010) 4066–4099.
[17] J. Liang, H. Zhao, Solving partial differential equations on point clouds, SIAM J. Sci. Comput. 35 (2013) A1461–A1486.
[18] D. Fortunato, A high-order fast direct solver for surface PDEs, SIAM J. Sci. Comput. 46 (2024) A2582–A2606.
[19] J. Beale, Solving partial differential equations on closed surfaces with planar cartesian grids, SIAM J. Sci. Comput. 42 (2020) A1052–A1070.
[20] C. Macdonald, S. Ruuth, The implicit closest point method for the numerical solution of partial differential equations on surfaces, SIAM J. Sci. Comput. 31 (2010) 4330–4350.
[21] C. Macdonald, S. Ruuth, Level set equations on surfaces via the closest point method, J. Sci. Comput. 35 (2008) 219–240.
[22] K. Deckelnick, G. Dziuk, C. Elliott, C. Heine, An h-narrow band finite-element method for elliptic equations on implicit surfaces, IMA J. Numer. Anal. 30 (2010) 351–376.
[23] M. Olshanskii, D. Safin, A narrow-band unfitted finite element method for elliptic PDEs posed on surfaces, Math. Comput. 85 (2016) 1549–1570.
[24] A. Reusken, Analysis of trace finite element methods for surface partial differential equations, IMA J. Numer. Anal. 35 (2015) 1568–1590.
[25] M. Olshanskii, A. Reusken, Trace finite element methods for PDEs on surfaces, in: Geometrically Unfitted Finite Element Methods and Applications: Proceedings of the UCL Workshop 2016, 2018, pp. 211–258.
[26] Z. Li, K. Ito, The immersed interface method: numerical solutions of PDEs involving interfaces and irregular domains, SIAM, 2006.
[27] Z. Li, M. Lai, The immersed interface method for the Navier–Stokes equations with singular forces, J. Comput. Phys. 171 (2001) 822–842.
[28] Y. Zhou, S. Zhao, M. Feig, G. Wei, High order matched interface and boundary method for elliptic equations with discontinuous coefficients and singular sources, J. Comput. Phys. 213 (2006) 1–30.
[29] S. Yu, Y. Zhou, G. Wei, Matched interface and boundary (MIB) method for elliptic problems with sharp-edged interfaces, J. Comput. Phys. 224 (2007) 729–756.
[30] W. Ying, C. Henriquez, A kernel-free boundary integral method for elliptic boundary value problems, J. Comput. Phys. 227 (2007) 1046–1074.
[31] W. Ying, W. Wang, A kernel-free boundary integral method for variable coefficients elliptic PDEs, Commun. Comput. Phys. 15 (2014) 1108–1140.
[32] H. Zhou, W. Ying, A correction function-based kernel-free boundary integral method for elliptic PDEs with implicitly defined interfaces, J. Comput. Phys. 496 (2024) 112545.
[33] L. Zhang, A. Gerstenberger, X. Wang, W. Liu, Immersed finite element method, Comput. Methods Appl. Mech. Eng. 193 (2004) 2051–2067.
[34] T. Lin, Y. Lin, X. Zhang, Partially penalized immersed finite element methods for elliptic interface problems, SIAM J. Numer. Anal. 53 (2015) 1121–1144.
[35] A. Mayo, The fast solution of Poisson's and the biharmonic equations on irregular regions, SIAM J. Numer. Anal. 21 (2) (1984) 285–299.
[36] A. Mayo, A decomposition finite difference method for the fourth order accurate solution of Poisson's equation on general regions, Int. J. High Speed Comput. 3 (2) (1991) 89–106.
[37] A. Mayo, A. Greenbaum, Fast parallel iterative solution of Poisson's and the biharmonic equations on irregular regions, SIAM J. Sci. Stat. Comput. 13 (1) (1992) 101–118.
[38] X. Xiao, X. Feng, Z. Li, The local tangential lifting method for moving interface problems on surfaces with applications, J. Comput. Phys. 431 (2021) 110146.
[39] C. Guo, X. Xiao, Z. Feng, X. &. Tan, An immersed finite element method for elliptic interface problems on surfaces, Comput. Math. Appl. 131 (2023) 54–67.
[40] J. Chen, X. Xiao, X. Feng, A mixed immersed finite element method for fourth-order interface problems on surfaces, Comput. Math. Appl. 176 (2024) 122–139.

[41] J. Chen, X. Xiao, X. Feng, D. Sheen, A level set immersed finite element method for parabolic problems on surfaces with moving interfaces, J. Comput. Phys. 531 (2025) 113939.

[42] T. Goodwill, M. O'neil, A parametrix method for elliptic surface PDEs, Pure Appl. Anal. 7 (2025) 171–217.

[43] M. Kropinski, N. Nigam, Fast integral equation methods for the Laplace-Beltrami equation on the sphere, Adv. Comput. Math. 40 (2014) 577–596.

[44] M. Kropinski, N. Nigam, B. Quaife, Integral equation methods for theLaplace-Beltrami equation on the sphere, Adv. Comput. Math. 42 (2016) 469–488.

[45] J. Barrett, H. Garcke, R. Nürnberg, Parametric finite element approximations of curvature-driven interface evolutions, Handb. Numer. Anal. 21 (2020) 275–423.

[46] J. Pan, J. Liu, Numerical solution of the boundary value problem of elliptic equation by Levi function scheme, Numer. Methods Partial Differ. Equ. 40 (2024) e23142.

[47] M. Mitrea, M. Taylor, Potential theory on Lipschitz domains in Riemannian manifolds: holder continuous metric tensors, Commun. Partial Differ. Equ. 25 (2000) 1487–1536.

[48] M. Mitrea, M. Taylor, Boundary layer methods for Lipschitz domains in Riemannian manifolds, J. Funct. Anal. 163 (1999) 181–251.

[49] W.C.H. McLean, Strongly Elliptic Systems and Boundary Integral Equations, Cambridge University Press, 2000.

[50] W. Hackbusch, Elliptic differential equations: theory and numerical treatment, Springer, 2017.

[51] T. Beale, A. Layton, On the accuracy of finite difference methods for elliptic problems with interfaces, Commun. Appl. Math. Comput. Sci. 1 (2007) 91–119.

[52] U. Trottenberg, C. Oosterlee, A. Schüller, Multigrid, Academic Press, 2001.

[53] W. Ying, W. Wang, A kernel-free boundary integral method for implicitly defined surfaces, J. Comput. Phys. 252 (2013) 606–624.